

1 LEVERAGING MULTI-MESSENGER ASTROPHYSICS FOR DARK MATTER SEARCHES

By

Daniel Nicholas Salazar-Gallegos

A DISSERTATION

Submitted to
Michigan State University
in partial fulfillment of the requirements
for the degree of

Physics—Doctor of Philosophy
Computational Mathematics in Science and Engineering—Dual Major

Today

ABSTRACT

3 I did Dark Matter with HAWC and IceCube. I also used Graph Neural Networks

⁴ Copyright by

⁵ DANIEL NICHOLAS SALAZAR-GALLEGOS

⁶ Today

ACKNOWLEDGMENTS

8 I love my friends. Thanks to everyone that helped me figure this out. Amazing thanks to the people
9 at LANL who supported me. Eames, etc Dinner Parties Jenny and her child Kaydince Kirsten, Pat,
10 Andrea Family. You're so far but so critical to my formation. Unconditional love. Roommate

TABLE OF CONTENTS

12	LIST OF TABLES	vii
13	LIST OF FIGURES	viii
14	LIST OF ABBREVIATIONS	xii
15	CHAPTER 1 INTRODUCTION	1
16	CHAPTER 2 DARK MATTER IN THE COSMOS	2
17	2.1 Introduction	2
18	2.2 Dark Matter Basics	3
19	2.3 Evidence for Dark Matter	4
20	2.4 Searching for Dark Matter: Particle DM	11
21	2.5 Sources for Indirect Dark Matter Searches	16
22	2.6 Multi-Messenger Dark Matter	18
23	CHAPTER 3 MULTIMESSENGER ASTROPHYSICS: DETECTING HIGH EN-	
24	ERGY NEUTRAL MESSENGERS	21
25	3.1 Introduction	21
26	3.2 Charged Particles in a Medium	21
27	3.3 Photons (γ)	22
28	3.4 Neutrinos (ν)	22
29	3.5 Opportunities to Combine for Dark Matter	22
30	CHAPTER 4 HIGH ALTITUDE WATER CHERENKOV (HAWC) OBSERVATORY .	24
31	4.1 The Detector	24
32	4.2 Events Reconstruction and Data Acquisition	24
33	4.3 Remote Monitoring	24
34	CHAPTER 5 ICECUBE NEUTRINO OBSERVATORY	25
35	5.1 The Detector	25
36	5.2 Events Reconstruction and Data Acquisition	25
37	5.3 Northern Test Site	25
38	CHAPTER 6 COMPUTATIONAL TECHNIQUES IN PARTICLE ASTROPHYSICS .	26
39	6.1 Neural Networks for Gamma/Hadron Separation	26
40	6.2 Parallel Computing for Dark Matter Analyses	26
41	CHAPTER 7 GLORY DUCK: MULTI-WAVELENGTH SEARCH FOR DARK MATT-	
42	TER ANNIHILATION TOWARDS DWARF SPHEROIDAL GALAX-	
43	IES	27
44	7.1 Introduction	27
45	7.2 Dataset and Background	29
46	7.3 Analysis	30

47	7.4	HAWC Results	36
48	7.5	Glory Duck Combined Results	37
49	7.6	Appendix: HAWC Systematics	41
50	7.7	<i>J</i> -factor distributions	45
51	7.8	Discussion and Conclusions	48
52	CHAPTER 8	NU DUCK	52
53	CHAPTER 9	MULTITHREADING HAWC ANALYSES FOR DARK MATTER	
54		SEARCHES	53
55	BIBLIOGRAPHY		54

LIST OF TABLES

<p>57 Table 7.1 Summary of the relevant properties of the dSphs used in the present work. 58 Column 1 lists the dSphs. Columns 2 and 3 present their heliocentric distance 59 and galactic coordinates, respectively. Columns 4 and 5 report the J-factors of 60 each source given from the \mathcal{GS} and \mathcal{B} independent studies and their estimated 61 $\pm 1\sigma$ uncertainties. The values $\log_{10} J$ (\mathcal{GS} set) [44] correspond to the mean 62 J-factor values for a source extension truncated at the outermost observed star. 63 The values $\log_{10} J$ (\mathcal{B} set) [46] are provided for a source extension at the tidal 64 radius of each dSph. Bolded sources are within HAWC's field of view and 65 provided to the Glory Duck analysis.</p>	<p style="margin-top: 150px;">33</p>
<p>66 Table 7.2 Summary of dSph observations by each experiment used in this work. A 67 ‘-’ indicates the experiment did not observe the dSph for this study. For 68 Fermi-LAT, the exposure at 1 GeV is given. For HAWC, $\Delta\theta$ is the absolute 69 difference between the source declination and HAWC latitude. HAWC is more 70 sensitive to sources with smaller $\Delta\theta$. For IACTs, we show the zenith angle 71 range, the total exposure, the energy range, the angular radius θ of the signal or 72 ON region, the ratio of exposures between the background-control (OFF) and 73 signal (ON) regions (τ), and the significance of gamma-ray excess in standard 74 deviations, σ.</p>	<p style="margin-top: 150px;">34</p>
<p>75 Proof I know how to include</p>	

LIST OF FIGURES

77	Figure 2.1	Rotation curve fit to NGC 6503 from [7]. Dashed line is the contribution 78 from visible matter. Dotted curves are from gas. Dash-dot curves are from 79 dark matter (DM). Solid line is the composite contribution from all matter 80 and DM sources. Data are indicated with bold dots with error bars. Data 81 agree strongly with a matter + DM composite prediction.	5
82	Figure 2.2	Light from distant galaxy is bent in unique ways depending on the distribution 83 of mass between the galaxy and Earth. Yellow dashed lines indicate where 84 the light would have gone if the matter were not present [8].	7
85	Figure 2.3	(left) Optical image of galactic cluster 1E0657-558. (right) X-ray image of the 86 cluster with redder meaning hotter and higher baryon density. (both) Green 87 contours are reconstruction of gravity contours from weak lensing. White 88 rings are the best fit mass maxima at 68.3%, 95.5%, and 99.7% confidence. 89 The matter maxima of the clusters are clearly separated from x-ray maxima. [9]	8
90	Figure 2.4	Plank CMB sky. Sky map features small variations in temperature in primor- 91 dial light. These anisotropies are used to make inferences about the universe's 92 energy budget and developmental history. [10]	9
93	Figure 2.5	Observed Cosmic Microwave Background power spectrum as a function of 94 multipole moment from Plank [10]. Blue line is best fit model from Λ CDM. 95 Red points and lines are data and error, respectively.	10
96	Figure 2.6	Predicted power spectra of CMB for different $\Omega_m h^2$ values for fixed baryon 97 density from [11]. (left) Low $\Omega_m h^2$ increases the prominence of first and 98 second peaks. (middle) $\Omega_m h^2$ is most similar to the observed power spectrum. 99 The second and third peaks are similar in height. (right) $\Omega_m h^2$ is large which 100 suppresses the first peak and raises the prominence of the third peak.	10
101	Figure 2.7	The Standard Model (SM) of particle physics. Figure taken from http://www.quantumdiaries.org/2014/03/14/the-standard-model-a-beautiful-but-flawed-theory/	12
104	Figure 2.8	Simplified Feynman diagram demonstrating with different ways DM can 105 interact with SM particles. The 'X's refer to the DM particles whereas the 106 SM refer to fundamental particles in the SM. The large circle in the center 107 indicates the vertex of interaction and is purposely left vague. The colored 108 arrows refer to different directions of time as well as their respective labels. 109 The arrows indicate the initial and final state of the DM -SM interaction in time.	13

110	Figure 2.9 A single jet event in ATLAS detector from 2017 [16]. Jet momentum was 111 observed to be 1.9 TeV. Missing transverse momentum was observed to be 112 1.9 TeV compared to the initial transverse momentum of the event was 0. 113 Implied MET is traced by a red dashed line in event display.	14
114	Figure 2.10 More detailed pseudo-Feynman diagram of particle cascade from dark matter 115 annihilation into 2 quarks. The quarks hadronize and down to stable particles 116 like γ or the anti-proton (p^-). Diagram pulled from ICRC 2021 presentation 117 on DM annihilation search [17].	15
118	Figure 2.11 Dark Matter (DM) decay spectrum for $b\bar{b}$ initial state and γ final state. Redder 119 spectra are for larger DM masses. Bluer spectra are light DM masses. x is a 120 unitless factor defined as the ratio of the mass of DM, m_χ , and the final state 121 particle energy E_γ . Figure from [19].	17
122	Figure 2.12 Different dark matter density profiles compared. Some models produce ex- 123 ceptionally large densities at small r [20].	18
124	Figure 2.13 The Milky Way Galaxy in photons (γ) and neutrinos (ν) [22]. The Galactic 125 center is at $l=0^\circ$ and is the brightest region in all panels. (top) An Optical 126 color image of the Milky Way galaxy seen from Earth. Clouds of gas and dust 127 obscure some light from stars. (2nd down) Integrated flux of γ -rays observed 128 by the Fermi-LAT telescope [23]. (middle) Expected neutrino emission 129 that corresponds with Fermi-LAT observations. (2nd up) Expected neutrino 130 emission profile after considering detector systematics of IceCube. (bottom) 131 Observed neutrino emission from region of the galactic plane. Substantial 132 neutrino emission was detected.	19
133	Figure 2.14 Dark Matter annihilation spectra for different final state particle and standard 134 model annihilation channels [24]. Photons (red), e^\pm (green), \bar{p} (blue), ν (black).	20
135	Figure 3.1 TODO: Show a nuclear reactor with cherenkov radiation[NEEDS A SOURCE][FACT 136 CHECK THIS]	22
137	Figure 3.2 TODO: absorption spectrum of liquid and solid water[NEEDS A SOURCE][FACT 138 CHECK THIS]	23

139	Figure 7.1 [NEEDS A SOURCE] Sensitivities of five gamma-ray experiments compared 140 to percentages of the Crab nebula's emission and dark matter annihilation. 141 Solid lines present estimated sensitivities to power law spectra [FACT CHECK 142 THIS] for each experiment. Green lines are Fermi-LAT sensitivities where 143 lighter green is the sensitivity to the galactic center and light green is its sen- 144 sitivity to higher declinations. Orange, red, and purple solid lines represent 145 the MAGIC, HESS, and VERITAS 50 hour sensitivities respectively. The 146 maroon and brown lines are the HAWC 1 year and 5 year sensitivities. Across 147 four decades of gamma-ray energy, these experiments have similar sensitiv- 148 ities on the order 10^{-12} erg cm $^{-2}$ s $^{-1}$. The dotted lines are estimated dark 149 matter fluxes assuming DM annihilating to bottom quarks (red), tau leptons 150 (blue), and W bosons (green). Faded grey lines outline percentage flux of the 151 Crab nebula.	27
152	Figure 7.2 TODO: figure from PPPC showing difference in pythia and ew correc- 153 tions.[NEEDS A SOURCE][FACT CHECK THIS]	31
154	Figure 7.3 Illustration of the combination technique showing a comparison between 155 $-2 \ln \lambda$ provided by four instruments (colored lines) from the observation 156 of the same dSph without any J nuisance and their sum, <i>i.e.</i> the resulting 157 combined likelihood (thin black line). According to the test statistics of 158 Equation (7.7), the intersection of the likelihood profiles with the line $-2 \ln \lambda$ 159 = 2.71 indicates the 95% C.L. upper limit on $\langle \sigma v \rangle$. The combined likeli- 160 hood (thin black line) shows a smaller value of upper limit on $\langle \sigma v \rangle$ than 161 those derived by individual instruments. We also show the uncertainties on 162 the J -factor affects the combined likelihood and degrade the upper limit on 163 $\langle \sigma v \rangle$ (thick black line). All likelihood profiles are normalized so that the 164 global minimum $\widehat{\langle \sigma v \rangle}$ is 0. We note that each profile depends on the observa- 165 tional conditions in which a target object was observed. The sensitivity of a 166 given instrument can be degraded and the upper limits less constraining if the 167 observations are performed in non optimal conditions such as a high zenith 168 angle or a short exposure time.	37
169	Figure 7.4 HAWC upper limits at 95% confidence level on $\langle \sigma v \rangle$ versus DM mass for 170 seven annihilation channels, using the set of J -factors from Ref. [47] The 171 solid line represents the observed combined limit. Dashed lines represent 172 limits from individual dSphs.	38
173	Figure 7.5 HAWC Brazil bands at 95% confidence level on $\langle \sigma v \rangle$ versus DM mass for 174 seven annihilation channels with J -factors from \mathcal{GS} [47]. The solid line 175 represents the combined limit from 13 dSphs. The dashed line is the expected 176 limit. The green band is the 68% containment. The yellow band is the 95% 177 containment.	39

178	Figure 7.6	Upper limits at 95% confidence level on $\langle \sigma v \rangle$ in function of the DM mass for 179 eight annihilation channels, using the set of J factors from Ref. [47] (\mathcal{GS} set 180 in Table 7.1). The black solid line represents the observed combined limit, 181 the black dashed line is the median of the null hypothesis corresponding 182 to the expected limit, while the green and yellow bands show the 68% and 183 95% containment bands. Combined upper limits for each individual detector 184 are also indicated as solid, colored lines. The value of the thermal relic 185 cross-section in function of the DM mass is given as the red dotted-dashed 186 line [52].	42
187	Figure 7.7	Same as Fig. 7.6, using the set of J factors from Ref. [46, 51] (\mathcal{B} set in Table 7.1).	43
188	Figure 7.8	Comparisons of the combined limits at 95% confidence level for each of the 189 eight annihilation channels when using the J factors from Ref. [47] (\mathcal{GS} set in 190 Table 7.1), plain lines, and the J factor from Ref. [46, 51] (\mathcal{B} set in Table 7.1), 191 dashed lines. The cross-section given by the thermal relic is also indicated [52].	44
192	Figure 7.9	Comparisons of the combined limits at 95% confidence level for a point source 193 analysis and extended source using [47] \mathcal{GS} J-factor distributions and PPPC 194 [43] annihilation spectra. Shown are the limits for Segue1 which will have 195 the most significant impact on the combined limit. 6 of the 7 DM annihilation 196 channels are shown. Solid lines are extended source studies. Dashed lines 197 are point source studies. Overall, the extended source analysis improves the 198 limit by a factor of 2.	45
199	Figure 7.10	Same as Fig. 7.9 on Coma Berenices. This dSph also contributes significantly 200 to the limit. The limits are identical in this case.	46
201	Figure 7.11	Comparison of combined limits when correcting for HAWC's pointing sys- 202 tematic. All DM annihilation channels are shown. The solid black line is the 203 ratio between published limit to the declination corrected limit. The blue solid 204 line or "Combined_og" represented the limits computed for Glory Duck. The 205 solid orange line or "Combined_ad" represented the limits computed after 206 correcting for the pointing systematic.	47
207	Figure 7.12	Comparisons between the J -factors versus the angular radius for the com- 208 putation of J factors from Ref. [47] (\mathcal{GS} set in Table 7.1) in blue and for 209 the computation from Ref. [46, 51] (\mathcal{B} set in Tab. 7.1) in orange. The solid 210 lines represent the central value of the J -factors while the shaded regions 211 correspond to the 1σ standard deviation.	49
212	Figure 7.13	Comparisons between the J -factors versus the angular radius for the com- 213 putation of J factors from Ref. [47] (\mathcal{GS} set in Tab. 7.1) in blue and for the 214 computation from Ref. [46, 51] (\mathcal{B} set in Tab. 7.1) in orange. The solid 215 lines represent the central value of the J -factors while the shaded regions 216 correspond to the 1σ standard deviation.	50

LIST OF ABBREVIATIONS

- 218 **MSU** Michigan State University
219 **LANL** Los Alamos National Laboratory
220 **DM** Dark Matter
221 **SM** Standard Model
222 **HAWC** High Altitude Water Cherenkov Observatory

223

CHAPTER 1

INTRODUCTION

224 Is the text not rendering right? Ah ok it knows im basically drafting the doc still

CHAPTER 2

225

DARK MATTER IN THE COSMOS

226 **2.1 Introduction**

227 The dark matter problem can be summarized in part by the following thought experiment.

228 Let us say you are the teacher for an elementary school classroom. You take them on a field
229 trip to your local science museum and among the exhibits is one for mass and weight. The exhibit
230 has a gigantic scale, and you come up with a fun problem for your class.

231 You ask your class, "What is the total weight of the classroom? Give your best estimation to
232 me in 30 minutes, and then we'll check your guess on the scale. If your guess is within 10% of the
233 right answer, we will stop for ice cream on the way back."

234 The students are ecstatic to hear this, and they get to work. The solution is some variation of
235 the following strategy. The students should give each other their weight or best guess if they do
236 not know. Then, all they must do is add each student's weight and get a grand total for the class.
237 The measurement on the giant scale should show the true weight of the class. When comparing
238 the measured weight to your estimation, multiply the measurement by 1.0 ± 0.1 to get the $\pm 10\%$
239 tolerances for your estimation.

240 Two of your students, Sandra and Mario, return to you with a solution.

241 They say, "We weren't sure of everyone's weight. We used 65 lbs. for the people we didn't
242 know and added everyone who does know. There are 30 of us, and we got 2,000 lbs.! That's a ton!"

243 You estimated 1,900 lbs. assuming the average weight of a student in your class was 60 lbs.
244 So, you are pleased with Sandra's and Mario's answer. You instruct your students to all gather on
245 the giant scale and read off the weight together. To all your surprise, the scale reads *10,000 lbs.*!
246 10,000 is significantly more than a 10% error from 2,000. In fact, it is approximately 5 times more
247 massive than either your or your students' estimates. You think to yourself and conclude there
248 must be something wrong with the scale. You ask an employee to check the scale and verify it is
249 well calibrated. They confirm that the scale is in working order. You weigh a couple of students
250 individually to assess that the scale is well calibrated. Sandra weighs 59 lbs., and Mario weighs

251 62 lbs., typical weights for their age. You then weigh each student individually and see that their
252 weights individually do not deviate greatly from 60 lbs. So, where does all the extra weight come
253 from?

254 This thought experiment serves as an analogy to the Dark Matter problem. The important
255 substitution to make however is to replace the students with stars and the classroom with a galaxy,
256 say the Milky Way. Individually the mass of stars is well measured and defined with the Sun as our
257 nearest test case. However, when we set out to measure the mass of a collection of stars as large as
258 galaxies, our well-motivated estimation is wildly incorrect. There simply is no way to account for
259 this discrepancy except without some unseen, or dark, contribution to mass and matter in galaxies.
260 I set out in my thesis to narrow the possibilities of what this Dark Matter could be.

261 This chapter is organized like the following... **TODO: Text should look like ... Chapter x has**
262 **blah blah blah.**

263 2.2 Dark Matter Basics

264 Presently, a more compelling theory of cosmology that includes Dark Matter (DM) in order
265 to explain a variety of observations is Λ Cold Dark Matter, or Λ CDM. I present the evidence
266 supporting Λ CDM in Section 2.3 yet discuss the conclusions of the Λ CDM model here. According
267 to Λ CDM fit to observations on the Cosmic Microwave Background (CMB), DM is 26.8% of the
268 universe's current energy budget. Baryonic matter, stuff like atoms, gas, and stars, contributes to
269 4.9% of the universe's current energy budget [1, 2, 3].

270 DM is dark; it does not interact readily with light at any wavelength. DM also does not interact
271 noticeably with the other standard model forces (Strong and Weak) at a rate that is readily observed
272 [3]. DM is cold, which is to say that the average velocity of DM is below relativistic speeds [1].
273 'Hot' DM would not likely manifest the dense structures we observe like galaxies, and instead
274 would produce much more diffuse galaxies than what is observed [3, 1]. DM is old; it played a
275 critical role in the formation of the universe and the structures within it [1, 2].

276 Observations of DM have so far been only gravitational. The parameter space available to what
277 DM could be therefore is extremely broad. The broad DM parameter space is iteratively tested in

278 DM searches by supposing a hypothesis that has not yet been ruled out and performing observations
279 to test them. When the observations yield a null result, the parameter space is constrained further.
280 I present some approaches for DM searches in Section 2.4.

281 **2.3 Evidence for Dark Matter**

282 Dark Matter (DM) has been a looming problem in physics for almost 100 years. Anomalies
283 have been observed by astrophysicists in galactic dynamics as early as 1933 when Fritz Zwicky
284 noticed unusually large velocity dispersion in the Coma cluster. Zwicky's measurement was the
285 first recorded to use the Virial theorem to measure the mass fraction of visible and invisible matter
286 in celestial bodies [4]. From Zwicky in [5], "*If this would be confirmed, we would get the surprising*
287 *result that dark matter is present in much greater amount than luminous matter.*" Zwicky's and
288 others' observation did not instigate a crisis in astrophysics because the measurements did not
289 entirely conflict with their understanding of galaxies [4]. In 1978, Rubin, Ford, and Norbert
290 measured rotation curves for ten spiral galaxies [6]. Rubin et al.'s 1978 publication presented a
291 major challenge to the conventional understanding of galaxies that could no longer be dismissed by
292 measurement uncertainties. Evidence has been mounting ever since for this exotic form of matter.
293 The following subsections provide three compelling pieces of evidence in support of the existence
294 of DM.

295 **2.3.1 First Clues: Stellar Velocities**

296 Zwicky, and later Rubin, measured the stellar velocities of various galaxies to estimate their
297 virial mass. The Virial Theorem upon which these observations are interpreted is written as

$$2T + V = 0. \quad (2.1)$$

298 Where T is the kinetic energy and V is the potential energy in a self-gravitating system. The
299 classical Newton's law of gravity from stars and gas was used for gravitational potential modeled in
300 the observed galaxies:

$$V = -\frac{1}{2} \sum_i \sum_{j \neq i} \frac{m_i m_j}{r_{ij}}. \quad (2.2)$$

301 Zwicky et al. measured just the velocities of stars apparent in optical wavelengths [5]. Rubin et al.
 302 added by measuring the velocity of the hydrogen gas via the 21 cm emission line of Hydrogen [6].
 303 The velocities of the stars and gas are used to infer the total mass of galaxies and galaxy clusters
 304 via Equation (2.1). An inferred mass is obtained from the luminosity of the selected sources. The
 305 two inferences are compared to each other as a luminosity to mass ratio which typically yielded [1]

$$\frac{M}{L} \sim 400 \frac{M_{\odot}}{L_{\odot}} \quad (2.3)$$

306 M_{\odot} and L_{\odot} referring to stellar mass and stellar luminosity, respectively. These ratios clearly indicate
 307 a discrepancy in apparent light and mass from stars and gas and their velocities.

308 Rubin et al. [6] demonstrated that the discrepancy was unlikely to be an underestimation of
 309 the mass of the stars and gas. The inferred "dark" mass was up to 5 times more than the luminous
 310 mass. This dark mass also needed to extend well beyond the extent of the luminous matter.

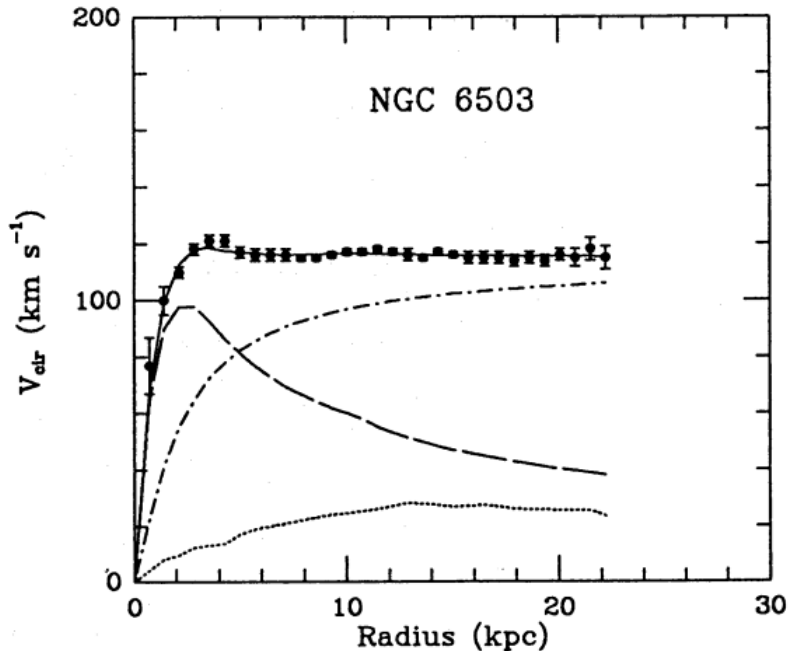


Figure 2.1 Rotation curve fit to NGC 6503 from [7]. Dashed line is the contribution from visible matter. Dotted curves are from gas. Dash-dot curves are from dark matter (DM). Solid line is the composite contribution from all matter and DM sources. Data are indicated with bold dots with error bars. Data agree strongly with a matter + DM composite prediction.

311 Figure 2.1 features one of many rotation curves plotted from the stellar velocities within galaxies.

312 The measured rotation curves mostly feature a flattening of velocities at higher radius which is not
313 expected if the gravity was only coming from gas and luminous matter. The extension of the
314 flat velocity region also indicates that the DM is distributed far from the center of the galaxy.
315 Modern velocity measurements include significantly larger objects, galactic clusters, and smaller
316 objects, dwarf galaxies. Yet, measurements along this regime are leveraging the Virial theorem
317 with Newtonian potential energies. We know Newtonian gravity is not a comprehensive description
318 of gravity. New observational techniques have been developed since 1978, and those are discussed
319 in the following sections.

320 **2.3.2 Evidence for Dark Matter: Gravitational Lensing**

321 Modern evidence for dark matter comes from new avenues beyond stellar velocities. Grav-
322 itational lensing from DM is a new channel from general relativity. General relativity predicts
323 aberrations in light caused by massive objects. In recent decades we have been able to measure the
324 lensing effects from compact objects and DM halos. Figure 2.2 shows how different massive ob-
325 jects change the final image of a faraway galaxy resulting from gravitational lensing. Gravitational
326 lensing developed our understanding of dark matter in two important ways.

327 Gravitational lensing provides additional compelling evidence for DM. The observation of two
328 merging galactic clusters in 2006, shown in Figure 2.3, provided a compelling argument for DM
329 outside the Standard Model. These clusters merged recently in astrophysical time scales. Galaxies
330 and star cluster have mostly passed by each other as the likelihood of their collision is low. Therefore,
331 these massive objects will mostly track the highest mass, dark and/or baryonic, density. Yet, the
332 intergalactic gas is responsible for the majority of the baryonic mass in the systems [4]. These gas
333 bodies will not phase through and will heat up as they collide together. The hot gas is located via
334 x-ray emission from the cluster. Two observations of the clusters were performed independently of
335 each other.

336 The first was the lensing of light around the galaxies due to their gravitational influences.
337 When celestial bodies are large enough, the gravity they exert bends space and time itself. The
338 warped space-time lenses light and will deflect in an analogous way to how glass lenses will bend

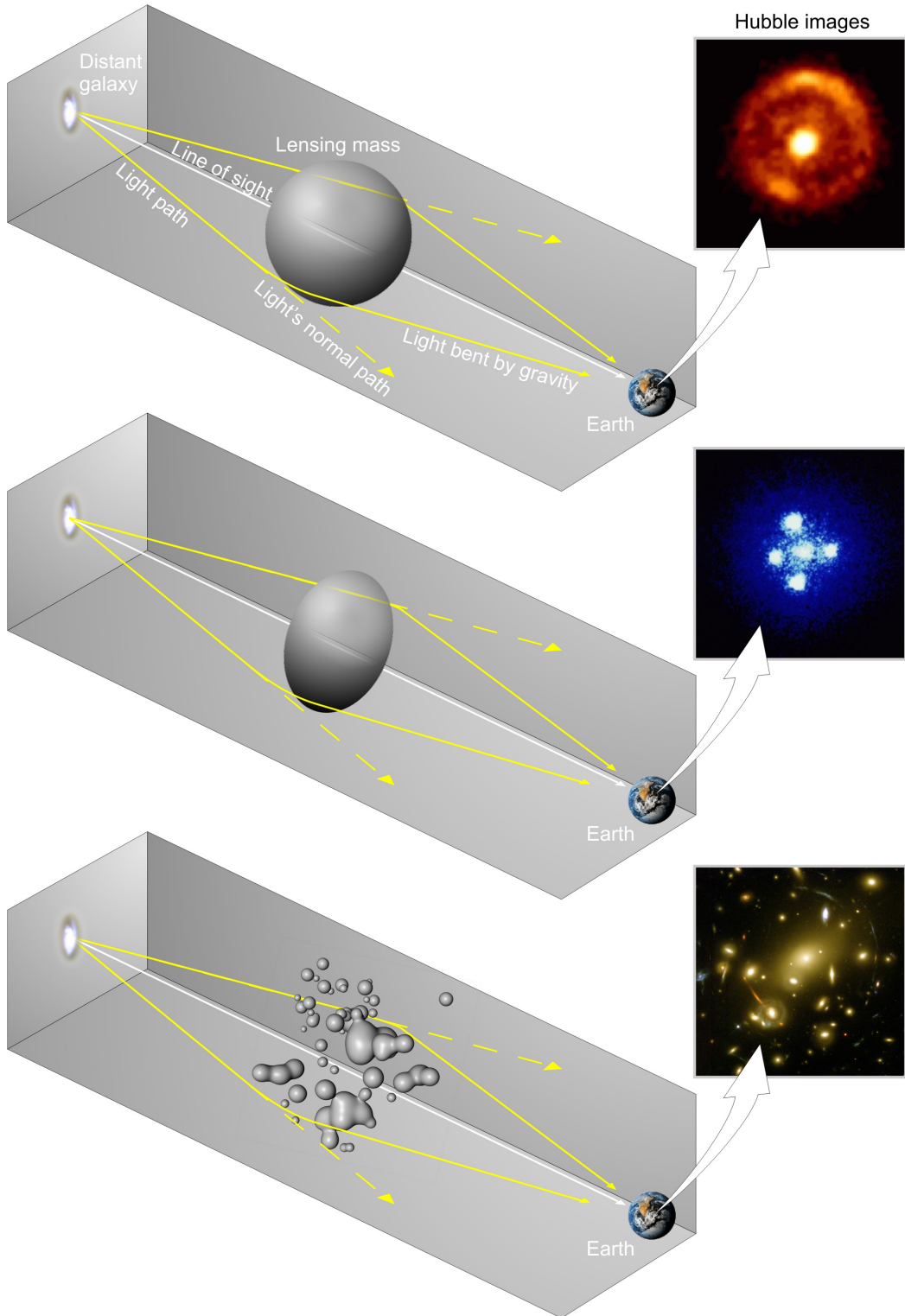


Figure 2.2 Light from distant galaxy is bent in unique ways depending on the distribution of mass between the galaxy and Earth. Yellow dashed lines indicate where the light would have gone if the matter were not present [8].

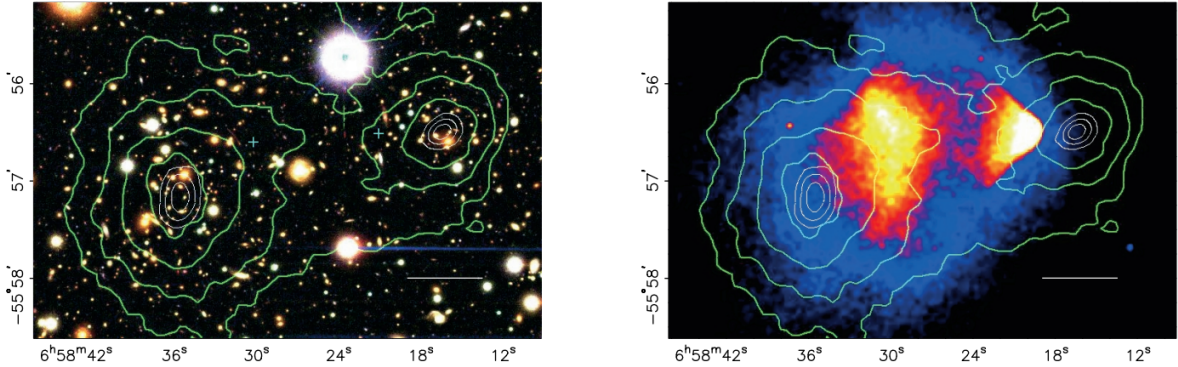


Figure 2.3 (left) Optical image of galactic cluster 1E0657-558. (right) X-ray image of the cluster with redder meaning hotter and higher baryon density. (both) Green contours are reconstruction of gravity contours from weak lensing. White rings are the best fit mass maxima at 68.3%, 95.5%, and 99.7% confidence. The matter maxima of the clusters are clearly separated from x-ray maxima. [9]

339 light, see Figure 2.2. With a sufficient understanding of light sources behind a massive object, we
 340 can reconstruct the contours of the gravitational lenses. The gradient of the contours shown in
 341 Figure 2.3 then indicates how dense the matter is and where it is.

342 The x-ray emission can then be observed from the clusters. Since these galaxies are mostly gas
 343 and are merging, then the gas should be getting hotter. If they are merging, the x-ray emissions
 344 should be the strongest where the gas is mostly moving through each other. Hence, X-ray emission
 345 maps out where the gas is in the merging galaxy cluster.

346 The lensing and x-ray observations were done on the Bullet cluster featured on Figure 2.3.
 347 The x-ray emissions do not align with the gravitational contours from lensing. The incongruence
 348 in mass density and baryon density suggests that there is a lot of matter somewhere that does
 349 not interact with light. Moreover, this dark matter cannot be baryonic [9]. The Bullet Cluster
 350 measurement did not really tell us what DM is exactly, but it did give the clue that DM also does
 351 not interact with itself very strongly. If DM did interact strongly with itself, then it would have been
 352 more aligned with the x-ray emission [9]. There have been follow-up studies of galaxy clusters with
 353 similar results. The Bullet Cluster and others like it provide a persuasive case against something
 354 possibly amiss in our gravitational theories.

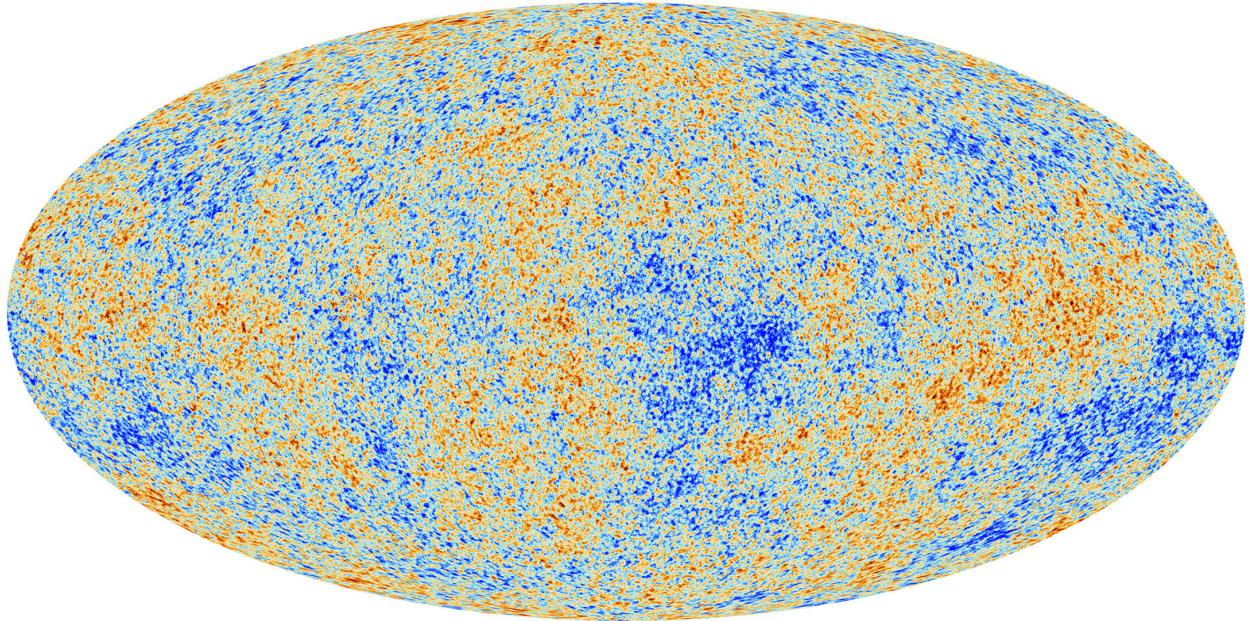


Figure 2.4 Plank CMB sky. Sky map features small variations in temperature in primordial light. These anisotropies are used to make inferences about the universe’s energy budget and developmental history. [10]

355 **2.3.3 Evidence for Dark Matter: Cosmic Microwave Background**

356 The Cosmic Microwave Background (CMB) is the primordial light from the early universe
357 when Hydrogen atoms formed from the free electron and proton soup in the early universe. The
358 CMB is the earliest light we can observe; released when the universe was about 380,000 years old.
359 Then we look at how the simulated universes look like compared to what we see. Figure 2.4 is the
360 most recent CMB image from the Plank satellite after subtracting the average value and masking the
361 galactic plane [10]. Redder regions indicate a slightly hotter region in the CMB, and blue indicates
362 colder. The intensity variations are on the order of 1 in 1000 with respect to the average value.

363 The Cosmic Microwave Background shows that the universe had DM in it from an incredibly
364 early stage. To measure the DM, Dark Energy, and matter fractions of the universe from the CMB,
365 the image is analyzed into a power spectrum, which shows the amplitude of the fluctuations as
366 a function of spherical multipole moments. Λ CDM provides the best fit to the power spectra of
367 the CMB as shown in Figure 2.5. The CMB power spectrum is quite sensitive to the fraction
368 of each energy contribution in the early universe. Low l modes are dominated by variations
369 in gravitational potential. Intermediate l emerge from oscillations in photon-baryon fluid from

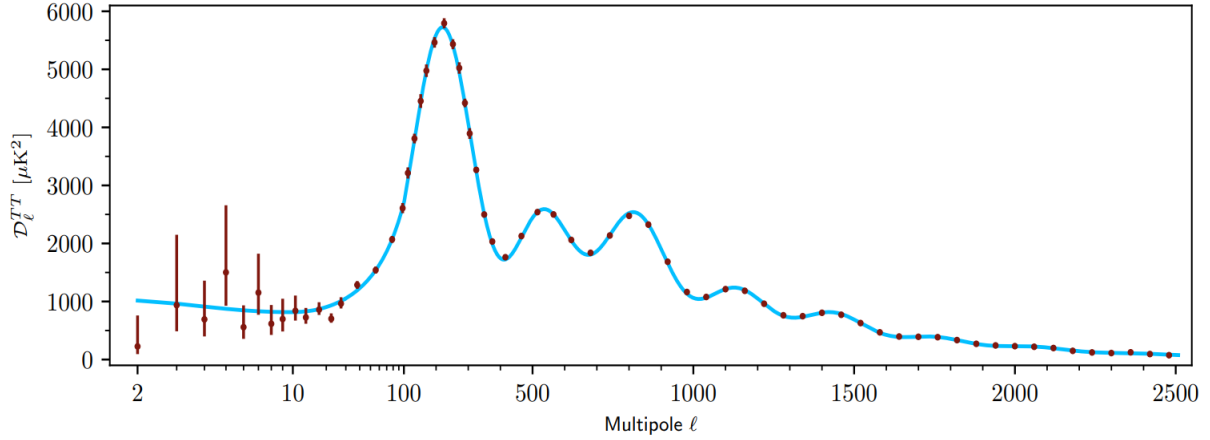


Figure 2.5 Observed Cosmic Microwave Background power spectrum as a function of multipole moment from Plank [10]. Blue line is best fit model from Λ CDM. Red points and lines are data and error, respectively.

370 competing baryon pressures and gravity. High l is a damped region from the diffusion of photons
 371 during electron-proton recombination. [1]

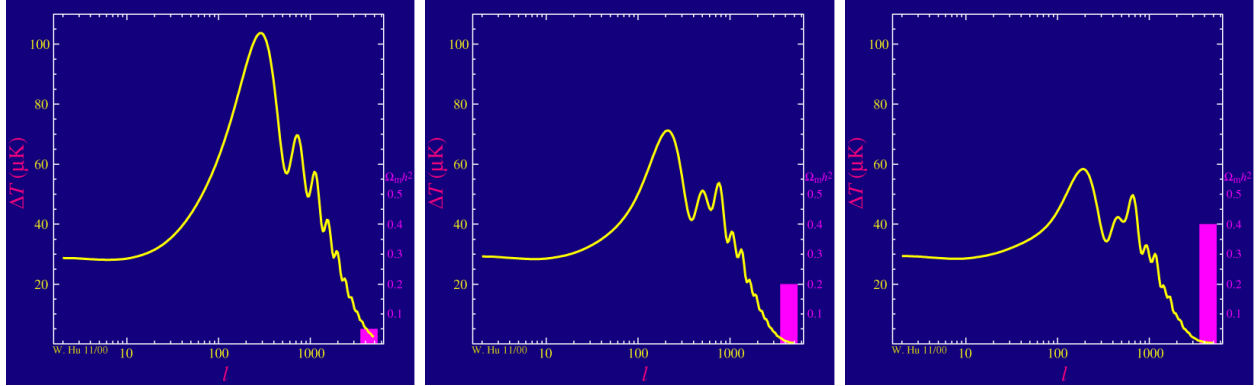


Figure 2.6 Predicted power spectra of CMB for different $\Omega_m h^2$ values for fixed baryon density from [11]. (left) Low $\Omega_m h^2$ increases the prominence of first and second peaks. (middle) $\Omega_m h^2$ is most similar to the observed power spectrum. The second and third peaks are similar in height. (right) $\Omega_m h^2$ is large which suppresses the first peak and raises the prominence of the third peak.

372 The harmonics would look quite different for a universe with less DM. Figure 2.6 demonstrates
 373 the effect $\Omega_m h^2$ has on the expected power spectrum for fixed baryon matter density. [11] Sweeping
 374 $\Omega_m h^2$ in this way clearly shows the effect dark matter has on the CMB power spectrum. The
 375 observations fit well with the Λ CDM model, and the derived fractions are as follows. The matter
 376 fraction: $\Omega_m = 0.3153$; and the baryon fraction: $\Omega_b = 0.04936$ [10]. Plank's observations also
 377 provide a measure of the Hubble constant, H_0 . H_0 especially has seen a growing tension in the

378 past decade that continues to deepened with observations from instruments like the James Webb
379 Telescope [12, 13]. As Hubble tensions deepen, we may find that perhaps Λ **CDM**, despite its
380 successes, is missing some critical physics.

381 Overall, the Newtonian motion of stars in galaxies, weak lensing from galactic clusters, and
382 power spectra from primordial light form a compelling body of research in favor of dark matter.
383 It takes another leap of theory and experimentation to make observations of DM that are non-
384 gravitational in nature. In Section 2.3, the evidence for DM implies strongly that the DM is matter
385 and not a lost parameter in the gravitational fields between massive objects. Finally, if we take one
386 axiom: that this matter has quantum behavior, such as being described by some Bohr wavelength
387 and abiding by some fermion or boson statistics; then we arrive at particle dark matter. One particle
388 DM hypothesis is the Weakly Interacting Massive Particle (WIMP). This DM candidate theory is
389 discussed further in the next section and is the focus of this thesis.

390 **2.4 Searching for Dark Matter: Particle DM**

391 Section 2.4 shows the Standard Model of particle physics and is currently the most accurate
392 model for the dynamics of fundamental particles like electrons and photons. The current status
393 of the SM does not have a viable DM candidate. When looking at the standard model, we can
394 immediately exclude any charged particle because charged particles interact strongly with light.
395 Specifically, this will rule out the following charged, fundamental particles: $e, \mu, \tau, W, u, d, s, c, t, b$
396 and their corresponding antiparticles. Recalling from Section 2.2 that DM must be long-lived and
397 stable over the age of the universe which excludes all SM particles with decay half-lives at or shorter
398 than the age of the universe. The lifetime constraint additionally eliminates the Z and H bosons.
399 Finally, the candidate DM needs to be somewhat massive. Recall from Section 2.2 that DM is cold
400 or not relativistic through the universe. This eliminates the remaining SM particles: $\nu_{e,\mu,\tau}, g, \gamma$ as
401 DM candidates. Because there are no DM candidates within the SM, the DM problem strongly
402 hints to physics beyond the SM (BSM).

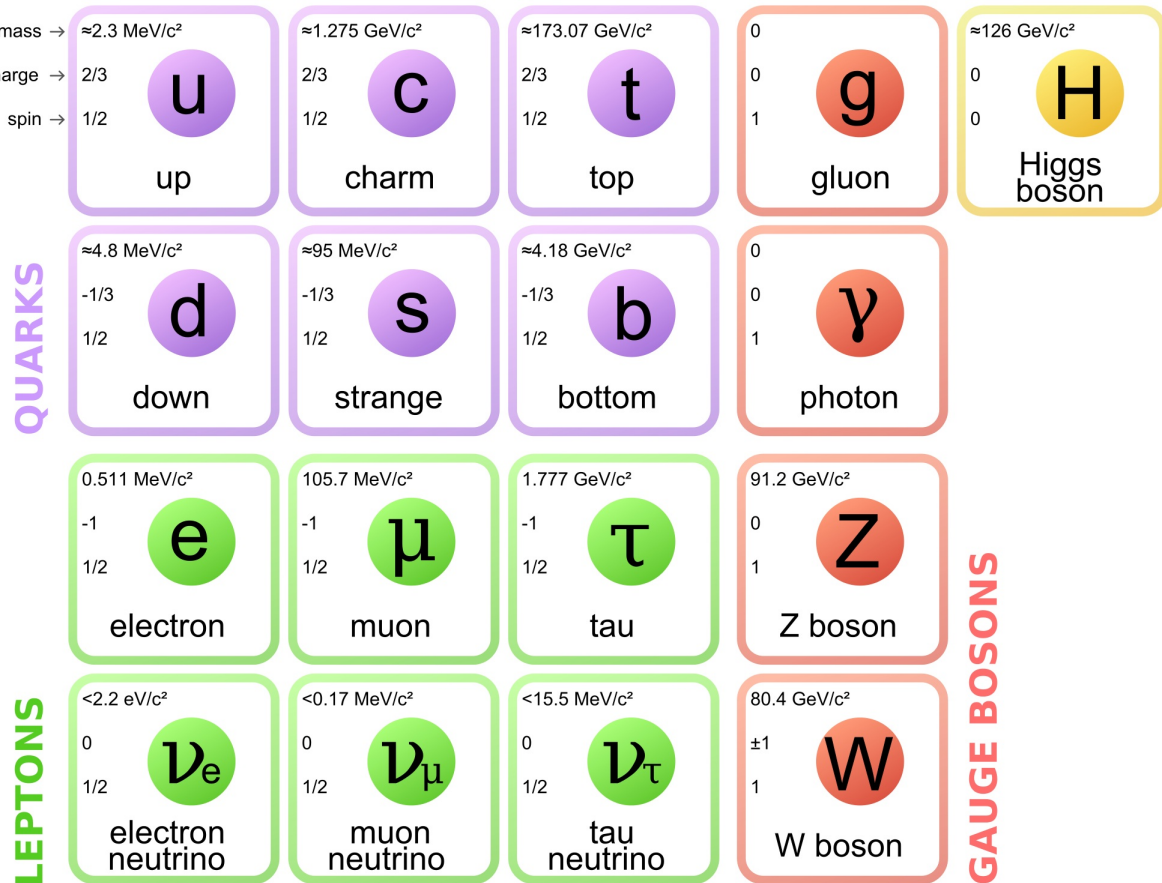


Figure 2.7 The Standard Model (SM) of particle physics. Figure taken from <http://www.quantumdiaries.org/2014/03/14/the-standard-model-a-beautiful-but-flawed-theory/>

403 2.4.1 Shake it, Break it, Make it

404 When considering DM that couples in some way with the SM, the interactions are roughly
 405 demonstrated by interaction demonstrated in Figure 2.8. The figure is a simplified Feynman
 406 diagram where the arrow of time represents the interaction modes of: **Shake it, Break it, Make it.**
 407 **Shake it** refers to the direct detection of dark matter. Direct detection interactions start with
 408 a free DM particle and an SM particle. The DM and SM interact via elastic or inelastic collision
 409 and recoil away from each other. The DM remains in the dark sector and imparts some momentum
 410 onto the SM particle. The hope is that the momentum imparted onto the SM particle is sufficiently
 411 high enough to pick up with extremely sensitive instruments. Because we cannot create the DM in
 412 the lab, a direct detection experiment must wait until DM is incident on the detector. Most direct
 413 detection experiments are therefore placed in low-background environments with inert detection

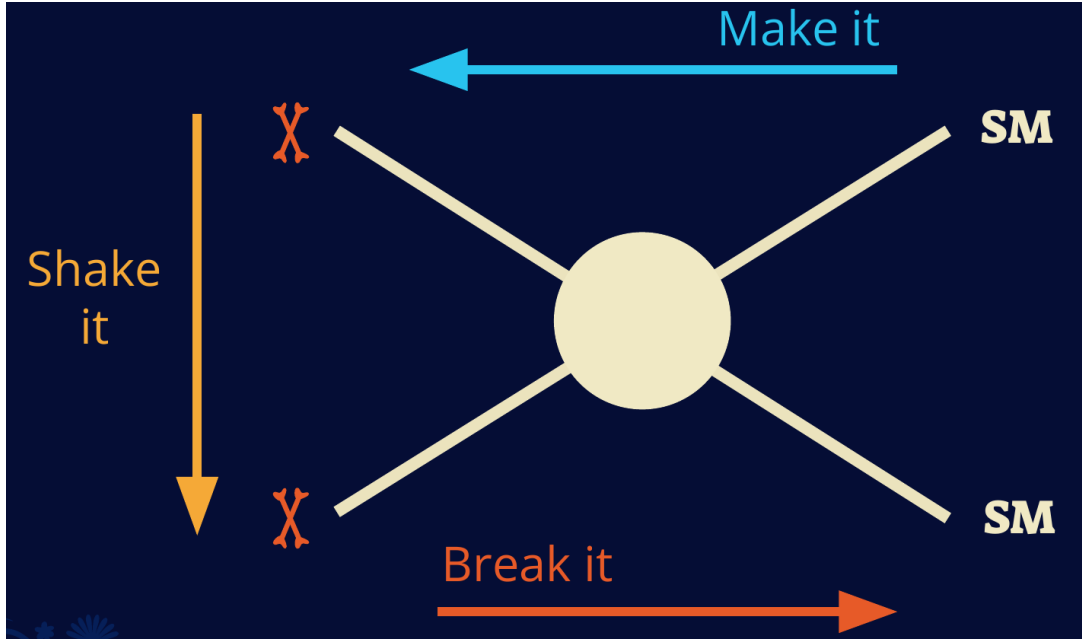


Figure 2.8 Simplified Feynman diagram demonstrating different ways DM can interact with SM particles. The 'X's refer to the DM particles whereas the SM refer to fundamental particles in the SM. The large circle in the center indicates the vertex of interaction and is purposely left vague. The colored arrows refer to different directions of time as well as their respective labels. The arrows indicate the initial and final state of the DM -SM interaction in time.

⁴¹⁴ media like the noble gas Xenon. [14]

⁴¹⁵ **Make it** refers to the production of DM from SM initial states. The experiment starts with
⁴¹⁶ particles in the SM. These SM particles are accelerated to incredibly high energies and then collide
⁴¹⁷ with each other. In the confluence of energy, DM hopefully emerges as a byproduct of the SM
⁴¹⁸ annihilation. Often it is the collider experiments that are energetic enough to hypothetically produce
⁴¹⁹ DM. These experiments include the world-wide collaborations ATLAS and CMS at CERN where
⁴²⁰ proton collide together at extreme energies. The DM searches, however, are complex. DM likely
⁴²¹ does not interact with the detectors and lives long enough to escape the detection apparatus of
⁴²² CERN's colliders. This means any DM production experiment searches for an excess of events
⁴²³ with missing momentum or energy in the events. An example event with missing transverse
⁴²⁴ momentum is shown in Figure 2.9. The missing momentum with no particle tracks implies a
⁴²⁵ neutral particle carried the energy out of the detector. However, there are other neutral particles
⁴²⁶ in the SM, like neutrons or neutrinos, so any analysis has to account for SM signatures of missing

427 momentum. [15]

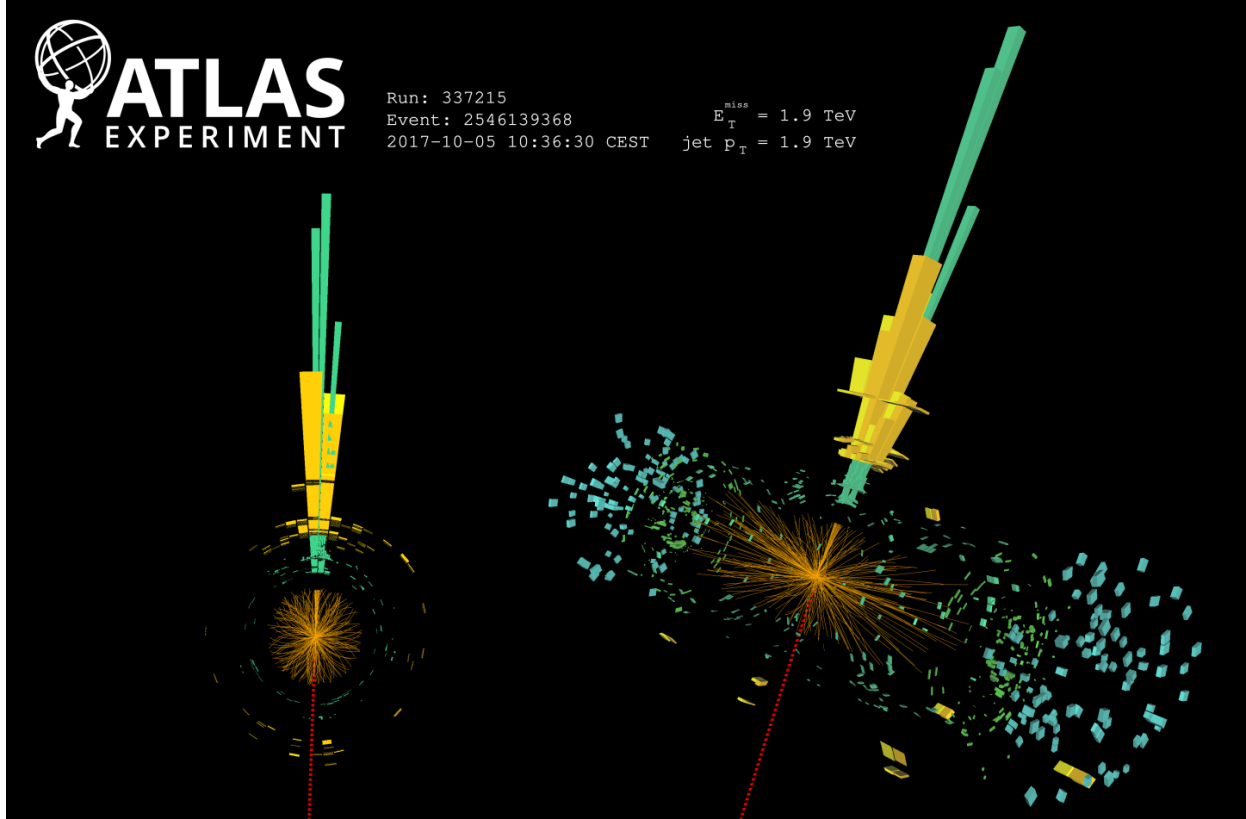


Figure 2.9 A single jet event in ATLAS detector from 2017 [16]. Jet momentum was observed to be 1.9 TeV. Missing transverse momentum was observed to be 1.9 TeV compared to the initial transverse momentum of the event was 0. Implied MET is traced by a red dashed line in event display.

428 2.4.2 Break it: Standard Model Signatures of Dark Matter through Indirect Searches

429 **Break it** refers to the creation of SM particles from the dark sector, and it is the primary focus
430 of this thesis. The interaction begins with DM or in the dark sector. The hypothesis is that this
431 DM will either annihilate with itself or decay and produce an SM byproduct. This method is
432 often referred to as the Indirect Detection of DM because we have no lab to directly control or
433 manipulate the DM. Therefore, most indirect DM searches are performed using observations of
434 known DM densities among the astrophysical sources. The strength is that we have the whole of the
435 universe and its 13.6-billion-year lifespan to use as a detector and particle accelerator. Additionally,
436 locations of dark matter are well cataloged since it was astrophysical observations that presented

437 the problem of DM in the first place.

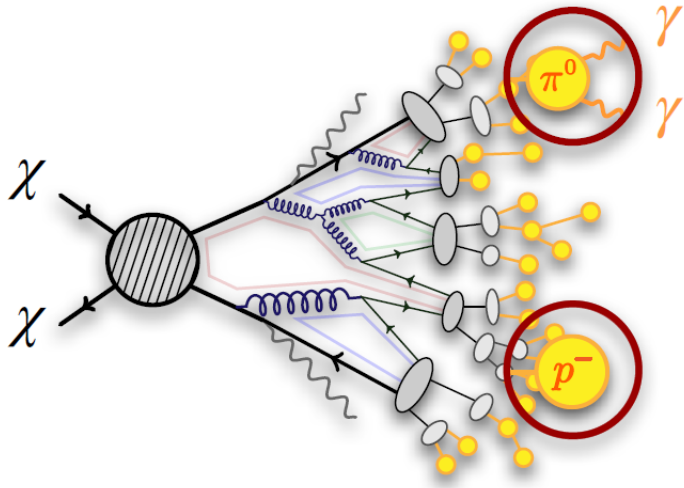


Figure 2.10 More detailed pseudo-Feynman diagram of particle cascade from dark matter annihilation into 2 quarks. The quarks hadronize and down to stable particles like γ or the anti-proton (p^-). Diagram pulled from ICRC 2021 presentation on DM annihilation search [17].

438 However, anything can happen in the universe. There are many difficult to deconvolve back-
439 grounds when searching for DM. One prominent example is the galactic center. We know the
440 galactic center has a large DM content because of stellar kinematics in our Milky Way and DM halo
441 simulations. Yet, any signal from the galactic center is challenging to parse apart from the extreme
442 environment of our supermassive black hole, unresolved sources, and diffuse emission from the
443 interstellar medium [18]. Despite the challenges, any DM model that yields evidence in the other
444 two observation methods, **Shake it or Make it** must be corroborated with indirect observations of
445 the known DM sources. Without corroborating evidence, DM observation in the lab is hard-pressed
446 to demonstrate that it is the model contributing to the DM seen at the universal scale.

447 In the case of WIMP DM, signals are described in terms of primary SM particles produced
448 from DM decay or annihilation. The SM initial state particles are then simulated down to stable
449 final states such as the γ , ν , p , or e which can traverse galactic lengths to reach Earth.

450 Figure 2.10 shows the quagmire of SM particles that emerges from SM initial states that are not
451 stable [17]. There are many SM particles with varying energies that can be produced in such an

452 interaction. For any arbitrary DM source and stable SM particle, the SM flux from DM annihilating
 453 to a neutral particle in the SM, ϕ , from a region in the sky is described by the following.

$$\frac{d\Phi_\phi}{dE_\phi} = \frac{\langle\sigma v\rangle}{8\pi m_\chi^2} \frac{dN_\phi}{dE_\phi} \times \int_{\text{source}} d\Omega \int_{l.o.s} \rho_\chi^2 dl(r, \theta') \quad (2.4)$$

454 In Equation (7.1), $\langle\sigma v\rangle$ is the velocity-weighted annihilation cross-section of DM to the SM. m_χ
 455 refers to the mass of DM, noted with Greek letter χ . $\frac{dN_\phi}{dE_\phi}$ is the N particle flux weighted by the
 456 particle energy. An example is provided in Figure 2.11 for the γ final state. The integrated terms
 457 are performed over the solid angle, $d\Omega$, and line of sight, l.o.s. ρ is the density of DM for a
 458 location (r, θ') in the sky. The terms left of the ' \times ' are often referred to as the particle physics
 459 component. The terms on the right are referred to as the astrophysical component. For decaying
 460 DM, the equation changes to...

$$\frac{d\Phi_\phi}{dE_\phi} = \frac{1}{4\pi\tau m_\chi} \frac{dN_\phi}{dE_\phi} \times \int_{\text{source}} d\Omega \int_{l.o.s} \rho_\chi dl(r, \theta') \quad (2.5)$$

461 In Equation (2.5), τ is the decay lifetime of the DM. Just as in Equation (7.1), the left and
 462 right terms are the particle physics and the astrophysical components respectively. The integrated
 463 astrophysical component of Equation (7.1) is often called the J-Factor. Whereas the integrated
 464 astrophysical component of Equation (2.5) is often called the D-Factor.

465 Exact DM $\text{DM} \rightarrow \text{SM SM}$ branching ratios are not known, so it is usually assumed to go 100%
 466 into an SM particle/anti-particle. Additionally, when a DM annihilation or decay produces one of
 467 the neutral, long-lived SM particles (ν or γ), the particle is traced back to a DM source. For DM
 468 above GeV energies, there are very few SM processes that can produce particles with such a high
 469 energy. Seeing such a signal would almost certainly be an indication of the presence of dark matter.
 470 Fortunately, the universe provides us with the largest volume and lifetime ever for a particle physics
 471 experiment.

472 2.5 Sources for Indirect Dark Matter Searches

473 The first detection of DM relied on optical observations. Since then, we have developed new
 474 techniques to find DM dense regions. As described in Section 2.3.1, many DM dense regions were
 475 through observing galactic rotation curves. Our Milky Way galaxy is among DM dense regions

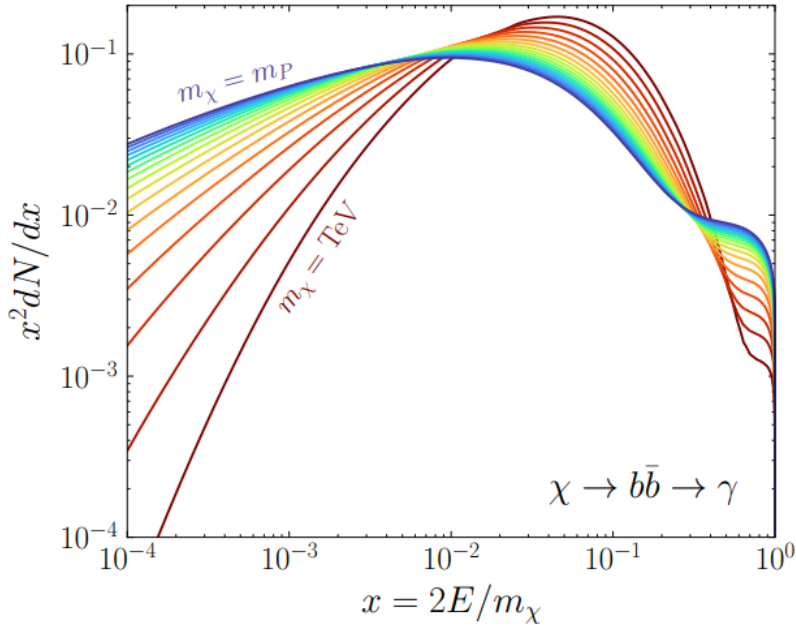


Figure 2.11 Dark Matter (DM) decay spectrum for $b\bar{b}$ initial state and γ final state. Redder spectra are for larger DM masses. Bluer spectra are light DM masses. x is a unitless factor defined as the ratio of the mass of DM, m_χ , and the final state particle energy E_γ . Figure from [19].

discovered, and it is the largest nearby DM dense region to look at. Additionally, the DM halo surrounding the Milky Way is clumpy [18]. There are regions in the DM halo of the Milky Way that have more DM than others that have captured gas over time. These sub-halos were dense enough collapse gas and form stars. These apparent sub galaxies are known as dwarf spheroidal galaxies and are the main sources studied in this thesis. Each source type comes with different trade-offs. Galactic Center studies will be very sensitive to the assumed distribution of DM. The central DM density can vary substantially as demonstrated in Figure 2.12. At distances close to the center of the galaxy, or small r , the differences in DM densities can be 3-4 orders of magnitude. Searches toward the galactic center will therefore be quite sensitive to the assumed DM distribution.

Searches toward Dwarf Spheroidal Galaxies (dSph's) suffer from uncertainties in the DM density less than the galactic center studies. This is mostly from their diminutive size being smaller than the angular resolution of most γ -ray observatories [18]. The DM content dSph's are typically determined with the Virial theorem, Equation (2.1), and are usually majority DM [18] in mass. DSph's tend to be ideal sources to look at for DM searches. Their environments are quiet with little

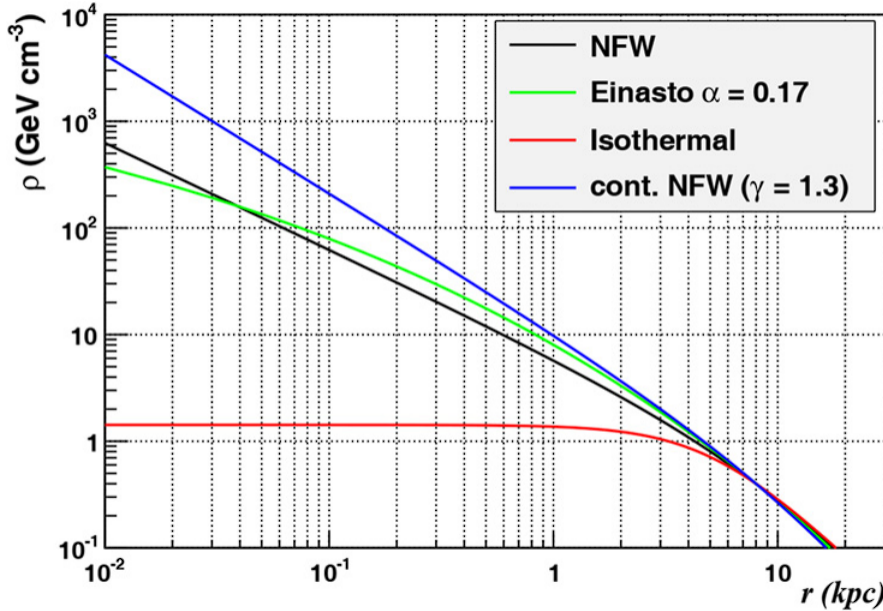


Figure 2.12 Different dark matter density profiles compared. Some models produce exceptionally large densities at small r [20].

490 astrophysical background. Unlike the galactic center, the most active components of dSph's are the
 491 stars within them versus a violent accretion disc around a black hole. All this together means that
 492 dSph's are among the best sources to look at for indirect DM searches. dSph's are the targets of
 493 focus for this thesis.

494 2.6 Multi-Messenger Dark Matter

495 Astrophysics entered a new phase in the past few decades that leverages our increasing sensitivity
 496 to SM channels and general relativity (GR). Up until the 21st century, astrophysical observations
 497 were performed with photons (γ) only. Astrophysics with this 'messenger' is fairly mature now.
 498 Novel observations of the universe have since only adjusted the sensitivity of the wavelength of
 499 light that is observed except at MeV energies. Gems like the CMB [10], and more have ultimately
 500 been observations of different wavelengths of light. Multi-messenger astrophysics proposes using
 501 other SM particles such the p^{+-} , or ν or gravitation waves predicted by general relativity.

502 The experiment LIGO had a revolutionary discovery in 2016 with the first detection of a binary
 503 black hole merger [21]. This opened the collective imagination to observing the universe through
 504 gravitational waves. There has also been a surge of interest in the neutrino (ν) sector. IceCube

505 demonstrated that we are sensitive to neutrinos in regions that correlate with significant photon
 506 emission like the galactic plane [22]. Neutrinos, like gravitational waves and light, travel mostly
 507 unimpeded from their source to our observatories. This makes pointing to the originating source
 508 of these messengers much easier than it is for cosmic rays which are deflected from their source by
 509 magnetic fields.

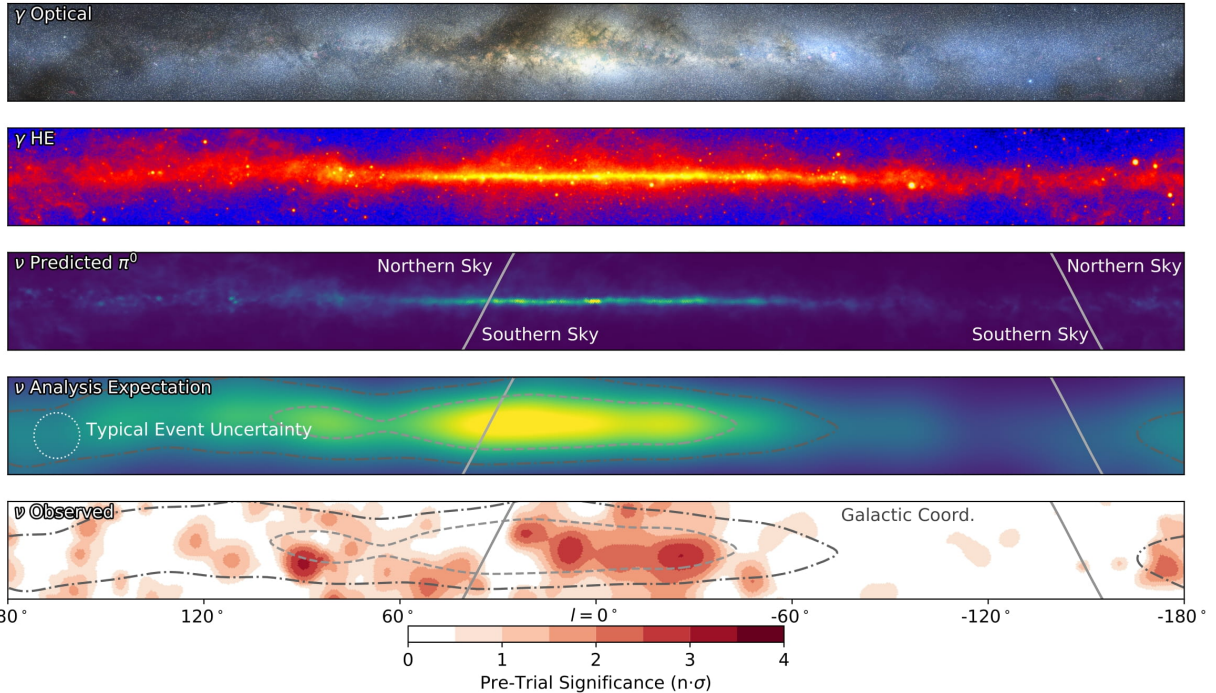


Figure 2.13 The Milky Way Galaxy in photons (γ) and neutrinos (ν) [22]. The Galactic center is at $l=0^\circ$ and is the brightest region in all panels. (top) An Optical color image of the Milky Way galaxy seen from Earth. Clouds of gas and dust obscure some light from stars. (2nd down) Integrated flux of γ -rays observed by the Fermi-LAT telescope [23]. (middle) Expected neutrino emission that corresponds with Fermi-LAT observations. (2nd up) Expected neutrino emission profile after considering detector systematics of IceCube. (bottom) Observed neutrino emission from region of the galactic plane. Substantial neutrino emission was detected.

510 The IceCube collaboration recently published a groundbreaking result of the Milky Way in
 511 neutrinos. The recent result from IceCube, shown in Figure 2.13, proves that we can make
 512 observations under different messenger regimes. The top two panels show the appearance of the
 513 galactic plane to different wavelengths of light. Some sources are more apparent in some panels,
 514 while others are not. This new channel is powerful because neutrinos are readily able to penetrate
 515 through gas and dust in the Milky Way. This new image also refines our understanding of how high

516 energy particles are produced. For example, the fit to IceCube data prefers neutrino production
 517 from the decay of π^0 [22].

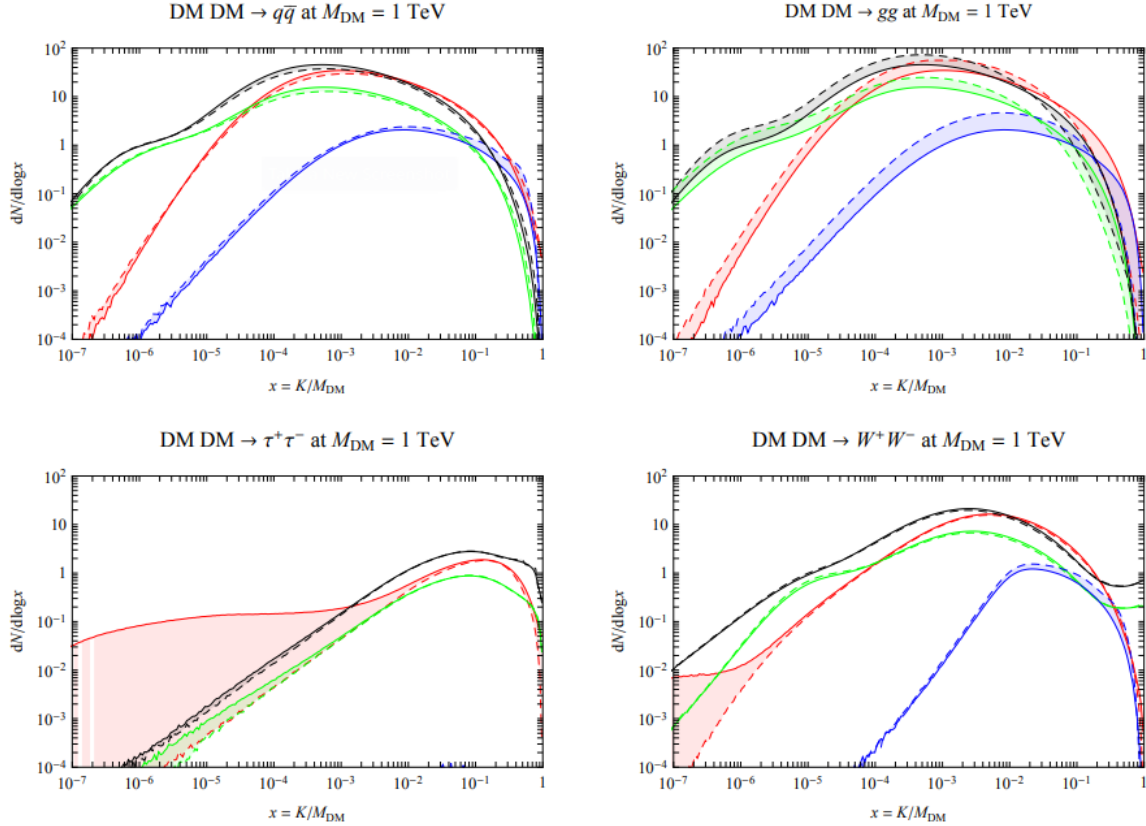


Figure 2.14 Dark Matter annihilation spectra for different final state particle and standard model annihilation channels [24]. Photons (red), e^\pm (green), \bar{p} (blue), ν (black).

518 Exposing our observations to more cosmic messengers greatly increases our sensitivity to
 519 rare processes. In the case of DM, Figure 2.14, there are many SM particles produced in DM
 520 annihilation. Among the final state fluxes are gammas and neutrinos. Charged particles are also
 521 produced however they would not likely make it to Earth since they will be deflected by magnetic
 522 fields between the source and Earth. This means observatories that can see the neutral messengers
 523 are especially good for DM searches and for combining data for a multi-messenger DM search.

CHAPTER 3

524 MULTIMESSENGER ASTROPHYSICS: DETECTING HIGH ENERGY NEUTRAL 525 MESSENGERS

526 3.1 Introduction

527 Before the 20th century, all asttrophysics observations were optical in nature. We litterly only
528 saw things with highly magnified optical observations. Then we discovered cosmic rays. cosmic
529 rays are charged particles, typically naked protons or H+. This was seen by Victor Hess in 19??.
530 Around the same time we discovered neutrinos from beta decay. Sometime around 1950 we started
531 to build neutrino detectors which were mostly sensitive to neutrinos from the sun. Finally, it was
532 theorized that compact objects like black holes and neutron stars would create waves in space-time
533 when they experience mergers or collisions.

534 In the 21st century, we have developed new observation techniques and detectors that are no only
535 sensitive to these four messengers - photons (TODO: photon), neutrinos (TODO: nu), Cosmic
536 Rays (CR), and Gravitational Wave (WV) - we're collect high energy versions of these events.
537 For the standad model particles, we're now sensitive to all messengers above the MeV eneryg
538 range. Additionally, the GW's were sensitive to are in the stellar mass black hole region and above
539 within our galactic neighborhood. This means were becoming sensitive to the fundamental physics
540 occuring within the universe and we can rely on the universe as a TeV+ particle accelerator. We
541 also have the abaility to correlate high energy events across messengers and gain new insights on
542 the processes that occur in our universe.

543 This thesis focuses on very high energy (VHE) gamma rays and neutrinos. These can both be
544 observed through the water cherenkov detection technique altho not exclusively. Methods on how
545 to detect and observe these neutral messengers are discussed Section 3.3 and Section 3.4

546 3.2 Charged Particles in a Medium

547 For high enery gamma-rays and neutrinos, we can exploit the same effect that charged particles
548 have with water. This effect is known as Cherenkov radiation. Cherenkov Radiation occurs when a
549 charged particle, usually electrons (e) or muons (μ), traverse a medium, like water, faster than the

550 speed of light in that medium. This is similar to sonic boom where an object moves through air
551 faster than the speed of sound in air. Cherenkov radiation can therefore be thought of as an 'optic
552 boom'. Many astro-particle physics experiments will use water as the medium as because water
553 has a unique set of properties ideal for charged particle tracking.



Figure 3.1 TODO: Show a nuclear reactor with cherenkov radiation[NEEDS A SOURCE][FACT CHECK THIS]

554 The frequency of light emitted due to cherenkov radiation follows the equation:

$$INSERT\ Cherenkov\ wavelength\ calc\ HERE. \quad (3.1)$$

555 The absorption spectra is shown in the following figure:

556 **3.3 Photons (γ)**

557 **3.4 Neutrinos (ν)**

558 **3.5 Opportunities to Combine for Dark Matter**



Figure 3.2 TODO: absorption spectrum of liquid and solid water[NEEDS A SOURCE][FACT CHECK THIS]

CHAPTER 4

559

HIGH ALTITUDE WATER CHERENKOV (HAWC) OBSERVATORY

560 **4.1 The Detector**

561 **4.2 Events Reconstruction and Data Acquisition**

562 **4.2.1 G/H Discrimination**

563 **4.2.2 Angle**

564 **4.2.3 Energy**

565 **4.3 Remote Monitoring**

566 **4.3.1 ATHENA Database**

567 **4.3.2 HOMER**

CHAPTER 5

ICECUBE NEUTRINO OBSERVATORY

569 **5.1 The Detector**

570 **5.2 Events Reconstruction and Data Acquisition**

571 **5.2.1 Angle**

572 **5.2.2 Energy**

573 **5.3 Northern Test Site**

574 **5.3.1 PIgeon remote dark rate testing**

575 **5.3.2 Bulkhead Construction**

CHAPTER 6

COMPUTATIONAL TECHNIQUES IN PARTICLE ASTROPHYSICS

577 **6.1 Neural Networks for Gamma/Hadron Separation**

578 **6.2 Parallel Computing for Dark Matter Analyses**

CHAPTER 7

GLORY DUCK: MULTI-WAVELENGTH SEARCH FOR DARK MATTER ANNIHILATION TOWARDS DWARF SPHEROIDAL GALAXIES

581 7.1 Introduction

582 The field of astrophysics now has several instruments and observatories sensitive to high
 583 energy gamma-rays. The energy sensitivity for the modern gamma-ray program spans many orders
 584 of magnitude. Figure 7.1 demonstrates these similar sensitivities across energies for the five
 585 experiments: Fermi-LAT, HAWC, HESS, MAGIC, and VERITAS.

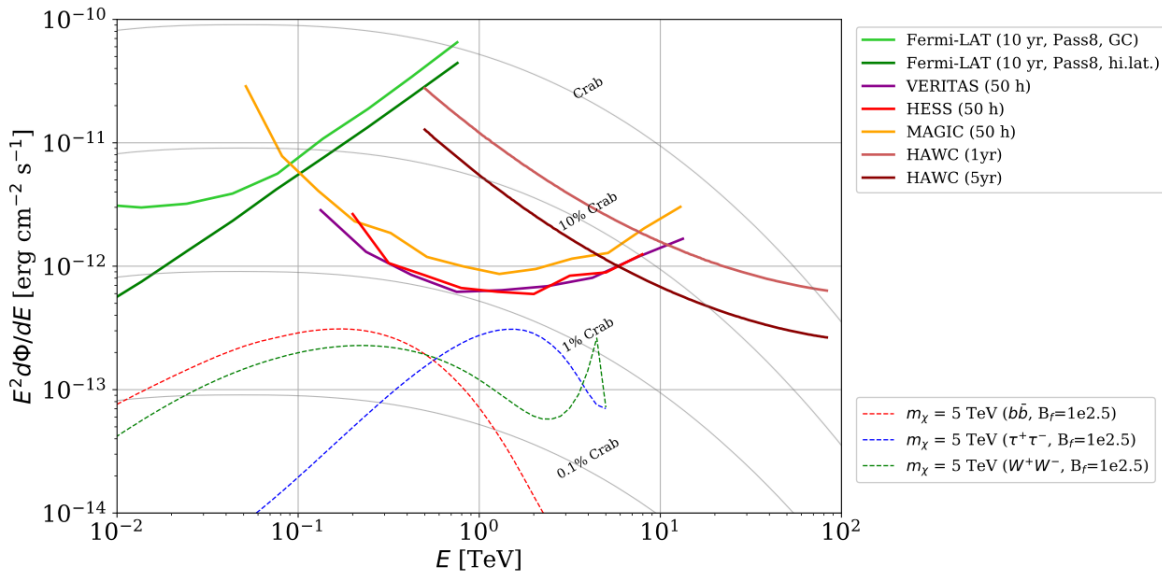


Figure 7.1 [NEEDS A SOURCE]Sensitivities of five gamma-ray experiments compared to percentages of the Crab nebula’s emission and dark matter annihilation. Solid lines present estimated sensitivities to power law spectra [FACT CHECK THIS]for each experiment. Green lines are Fermi-LAT sensitivities where lighter green is the sensitivity to the galactic center and light green is its sensitivity to higher declinations. Orange, red, and purple solid lines represent the MAGIC, HESS, and VERITAS 50 hour sensitivities respectively. The maroon and brown lines are the HAWC 1 year and 5 year sensitivities. Across four decades of gamma-ray energy, these experiments have similar sensitivities on the order 10^{-12} erg cm $^{-2}$ s $^{-1}$. The dotted lines are estimated dark matter fluxes assuming DM annihilating to bottom quarks (red), tau leptons (blue), and W bosons (green). Faded grey lines outline percentage flux of the Crab nebula.

586 Each of the five experiments featured in Figure 7.1 have independently searched for DM
 587 annihilation from dwarf galaxies and set limits. Intriguingly, their similarities overlap in regions
 588 where these observatories are less sensitive. This clearly motivates an analysis that combines data

589 from these five. Each experiment has unique gamma-ray detection methods and their weaknesses
590 and strengths can be leveraged with each other. The HAWC gamma-ray observatory is extensively
591 introduced in chapter 4, so it is not introduced here. A brief description of the remaining experiments
592 are in the following paragraphs.

593 The Large Area Telescope (LAT) is a pair conversion telescope mounted on the NASA Fermi
594 satellite in orbit 550 km above the Earth [25]. LAT's field of view covers about 20% of the
595 whole sky, and it sweeps the whole sky every 3 hours, approximately. LAT's gamma-ray energy
596 sensitivity ranges from 20 MeV up to 1 TeV. Previous DM searches towards dwarf galaxies using
597 Fermi-LAT are published in [26] and [27]

598 The High Energy Spectroscopic System (HESS), Major Atmospheric Gamma Imaging
599 Cherenkov (MAGIC), and Very Energetic Radiation Imaging Telescope Array System (VERI-
600 TAS) are arrays of Imaging Atmospheric Cherenkov Telescopes (IACT). These telescopes observe
601 the Cherenkov light emitted from gamma-ray showers in the Earth's atmosphere. The field for
602 these telescopes is no larger than 5° with energy sensitivities ranging from 30 GeV up to 100 TeV.
603 [28, 29, 30] IACTs are able to make precise observations in selected regions of the sky, however
604 can only be operated in ideal dark conditions. HESS's observations of the dwarves Sculptor and
605 Carina were between January 2008 and December 2009. HESS observations of Coma Berenices
606 were from 2010 to 2013, and Fornax was observed in 2010 [31, 32, 33]. MAGIC provided deep
607 observations of Segue1 between 2011 and 2013 [34]. MAGIC also provides data for three dwarves:
608 Coma Berenices, Draco, and Ursa Major II where observations were made in: January - June 2019
609 [35], March - September 2018 [35], and 2014 - 2016 [36] respectively. VERITAS provided data
610 for Boötes I, Draco, Segue 1, and Ursa Minor from 2009 to 2016 [37]

611 This chapter presents the Glory Duck analysis, the name given for the search for dark matter
612 annihilation from dwarf galaxies by combining data from the five gamma-ray observatories: Fermi-
613 LAT, HAWC, HESS, MAGIC, and VERITAS. Specifically, the methods in analysis and modeling
614 are presented for the HAWC gamma-ray observatory. This work was published to ??? and presented
615 at the International Cosmic Ray Conference in 2019, 2021, and 2023 [38, 39, 40] and more.

616 **7.2 Dataset and Background**

617 This section enumerates the data and background methods used for HAWC's study of the dwarf
618 spheroidal galaxies (dSph). Section 7.2.1 and Section 7.2.2 are most useful for fellow HAWC
619 collaborators looking to replicate the Glory Duck analysis.

620 **7.2.1 Itemized HAWC files**

- 621 • Detector Resolution: [response_aerie_svn_27754_systematics_best_mc_test_no](#)
622 [broadpulse_10pctlogchargesmearing_0.63qe_25kHzNoise_run5481_curvatu](#)
623 [re0_index3.root](#)
- 624 • Data Map: [maps-20180119/liff/maptree_1024.root](#)
- 625 • Spectral Dictionary: [DM_CirrelliSpectrum_dict_gammas.npy](#)
- 626 • Analysis wiki: https://private.hawc-observatory.org/wiki/index.php/Glory_Duck_Multi-Experiment_Dark_Matter_Search

628 **7.2.2 Software Tools and Development**

629 This analysis was performed using HAL and 3ML, in Python version 2[41, 42]. I built software
630 to implement the *Poor Particle Physicists' Cookbook* (PPPC) [43] DM spectral model and dSphs
631 spatial model from [44] for HAWC analysis. A NumPy version of this dictionary was made for
632 both Py2 and Py3. The code base for creating this dictionary is linked on my GitLab sandbox:

- 633 • Py2: [Dictionary Generator \(Deprecated\)](#)
- 634 • Py3: [PPPC2Dict](#)

635 The analysis was performed using the f_{hit} framework performed in the Crab paper[41]. The
636 Python2 NumPy dictionary file for gamma-ray final states is [dmCirSpecDict.npy](#). The corre-
637 sponding Python3 file is [DM_CirrelliSpectrum_dict_gammas.npy](#). These files can also be
638 used for decay channels and the PPPC describes how. [43]. All other software used for data

639 analysis, DM profile generation, and job submission to SLURM are also kept in my sandbox for
640 the Glory Duck project.

641 **7.2.3 Data Set and Background Description**

642 The HAWC data maps used for this analysis contain 1017 days of data between runs 2104
643 (2014-11-26) and 7476 (2017-12-20). They were generated from pass 4.0 reconstruction. The
644 analysis is performed using the f_{hit} energy binning scheme with bins (1-9) similar to what was done
645 for the Crab and previous HAWC dSph analysis. [41, 45]. Bin 0 was excluded as it has substantial
646 hadronic contamination and poor angular resolution.

647 This analysis was done on dwarf spheroidal (dSph) galaxies because of their large dark matter
648 (DM) content relative to baryonic. We consider the following to estimate the background to this
649 study.

- 650 • The dSphs are small in HAWC’s field of view, so the analysis is not sensitive to large or small
651 scale anisotropies.
- 652 • The dSphs used in this analysis are off the galactic plane.
- 653 • The dSphs are baryonically faint relative to their expected dark matter content and are not
654 expected to contain gamma-ray sources.

655 Therefor we make no additional assumptions on the background from our sources and use
656 HAWC’s standard direct integration method for background estimation [41]. It is possible for
657 gamma rays from DM annihilation to scatter in transit to HAWC via Inverse Compton Scattering
658 (ICS). This was investigated and its impact on the flux is basically zero. Supporting information
659 on this is in [TODO: refer to appdx](#)

660 **7.3 Analysis**

661 The expected differential photon flux from DM-DM annihilation to standard model particles
662 over solid angle is described by the familiar equation.

$$\frac{d\Phi_\gamma}{dE_\gamma} = \frac{\langle\sigma v\rangle}{8\pi m_\chi^2} \frac{dN_\gamma}{dE_\gamma} \times \int_{\text{source}} d\Omega \int_{l.o.s} \rho_\chi^2 dl(r, \theta') \quad (7.1)$$

663 Where $\langle \sigma v \rangle$ is the velocity weighted annihilation cross-section. $\frac{dN}{dE}$ is the expected differential
664 number of photons produced at each energy per annihilation. M_χ is the rest mass of the supposed
665 DM particle. J is the astrophysical J-factor and is defined as

$$J = \int \int \rho_\chi^2(l, \Omega) dl d\Omega \quad (7.2)$$

666 ρ_χ is the DM density. How each component is generated and considered for HAWC's analysis
667 is presented in the following sections.

668 **7.3.1 $\frac{dN_\gamma}{dE_\gamma}$ Particle Physics Component**

669 For this value, we import the PPPC with electroweak corrections [43]. The spectrum is
670 implemented as a model script in astromodels for 3ML. The PPPC model selected for this analysis
671 included electroweak corrections. The electroweak corrections were previously not considered for
HAWC and are significant for DM annihilating to **TODO: fill in SM particles**[45].



Figure 7.2 **TODO: figure from PPPC showing difference in pythia and ew corrections.[NEEDS A SOURCE][FACT CHECK THIS]**

672

673 The class in atromodels created to include the PPPC is aptly named `PPPCSpectra` within
674 `DM_models.py`.

675 The J-factor profiles for each source is imported from Geringer-Sameth (\mathcal{GS}) [44]. Another
676 DM distribution model from Bonnivard (\mathcal{B}) [46] was used for the complete study. However, to
677 save computational time, limits from \mathcal{GS} were scaled to \mathcal{B} instead of each experiment performing
678 a full study a second time. We create NSIDE 16384 maps of the J-factors for each dSph. These
679 maps are integrated over every spatial bin and passed to the fitting software. Plots of these maps
680 are provided for each source in the sandbox directory: `GD_mass_profiles`.

681 **7.3.2 Source Selection and Annihilation Channels**

682 We use many of the dSph presented in our previous dSph DM search [45]. HAWC’s sources
683 for Glory Duck include Boötes I, Coma Berenices, Canes Venatici I + II, Draco, Hercules, Leo I,
684 II, + IV, Segue 1, Sextans, and Ursa Major I + II. A full description of all sources used in Glory
685 Duck is found in Table 7.1. Triangulum II was excluded from the Glory Duck analysis because
686 of large uncertainties in its J-factor. Ursa Minor was excluded from HAWC’s contribution to the
687 combination because the source extension model extended Ursa Minor beyond HAWC’s field of
688 view. Ursa Minor was not expected to contribute significantly to the combined limit, so work was
689 not invested in a solution to include Ursa Minor.

690 The DM annihilation channels probed for the Glory Duck combination include $b\bar{b}$, $e\bar{e}$, $\mu\bar{\mu}$, $\tau\bar{\tau}$,
691 $t\bar{t}$, W^+W^- , and ZZ . A summary of all sources, with a description of each experiments’ sensitivity
692 to the source, is provided in Table 7.2.

693 **7.3.3 Likelihood Methods**

694 We perform a standard HAWC binned maximum likelihood analysis using f_{hit} bins 1-9. This
695 analysis was performed using HAL and 3ML, in Python2 [41, 42]. With these tools we compute
696 the max from the likelihood profiles and perform a ratio test to calculate the significance of each
697 source. This analysis is identical to the previous dSph analysis [45] except the sources are treated
698 as extended. For the vast majority of our sources, this extension is no greater than 2 degrees. We

Table 7.1 Summary of the relevant properties of the dSphs used in the present work. Column 1 lists the dSphs. Columns 2 and 3 present their heliocentric distance and galactic coordinates, respectively. Columns 4 and 5 report the J -factors of each source given from the \mathcal{GS} and \mathcal{B} independent studies and their estimated $\pm 1\sigma$ uncertainties. The values $\log_{10} J$ (\mathcal{GS} set) [44] correspond to the mean J -factor values for a source extension truncated at the outermost observed star. The values $\log_{10} J$ (\mathcal{B} set) [46] are provided for a source extension at the tidal radius of each dSph. **Bolded sources are within HAWC's field of view and provided to the Glory Duck analysis.**

Name	Distance (kpc)	l, b ($^{\circ}$)	$\log_{10} J$ (\mathcal{GS} set) $\log_{10}(\text{GeV}^2\text{cm}^{-5}\text{sr})$	$\log_{10} J$ (\mathcal{B} set) $\log_{10}(\text{GeV}^2\text{cm}^{-5}\text{sr})$
Boötes I	66	358.08, 69.62	$18.24^{+0.40}_{-0.37}$	$18.85^{+1.10}_{-0.61}$
Canes Venatici I	218	74.31, 79.82	$17.44^{+0.37}_{-0.28}$	$17.63^{+0.50}_{-0.20}$
Canes Venatici II	160	113.58, 82.70	$17.65^{+0.45}_{-0.43}$	$18.67^{+1.54}_{-0.97}$
Carina	105	260.11, -22.22	$17.92^{+0.19}_{-0.11}$	$18.02^{+0.36}_{-0.15}$
Coma Berenices	44	241.89, 83.61	$19.02^{+0.37}_{-0.41}$	$20.13^{+1.56}_{-1.08}$
Draco	76	86.37, 34.72	$19.05^{+0.22}_{-0.21}$	$19.42^{+0.92}_{-0.47}$
Fornax	147	237.10, -65.65	$17.84^{+0.11}_{-0.06}$	$17.85^{+0.11}_{-0.08}$
Hercules	132	28.73, 36.87	$16.86^{+0.74}_{-0.68}$	$17.70^{+1.08}_{-0.73}$
Leo I	254	225.99, 49.11	$17.84^{+0.20}_{-0.16}$	$17.93^{+0.65}_{-0.25}$
Leo II	233	220.17, 67.23	$17.97^{+0.20}_{-0.18}$	$18.11^{+0.71}_{-0.25}$
Leo IV	154	265.44, 56.51	$16.32^{+1.06}_{-1.70}$	$16.36^{+1.44}_{-1.65}$
Leo V	178	261.86, 58.54	$16.37^{+0.94}_{-0.87}$	$16.30^{+1.33}_{-1.16}$
Leo T	417	214.85, 43.66	$17.11^{+0.44}_{-0.39}$	$17.67^{+1.01}_{-0.56}$
Sculptor	86	287.53, -83.16	$18.57^{+0.07}_{-0.05}$	$18.63^{+0.14}_{-0.08}$
Segue I	23	220.48, 50.43	$19.36^{+0.32}_{-0.35}$	$17.52^{+2.54}_{-2.65}$
Segue II	35	149.43, -38.14	$16.21^{+1.06}_{-0.98}$	$19.50^{+1.82}_{-1.48}$
Sextans	86	243.50, 42.27	$17.92^{+0.35}_{-0.29}$	$18.04^{+0.50}_{-0.28}$
Ursa Major I	97	159.43, 54.41	$17.87^{+0.56}_{-0.33}$	$18.84^{+0.97}_{-0.43}$
Ursa Major II	32	152.46, 37.44	$19.42^{+0.44}_{-0.42}$	$20.60^{+1.46}_{-0.95}$
Ursa Minor	76	104.97, 44.80	$18.95^{+0.26}_{-0.18}$	$19.08^{+0.21}_{-0.13}$

Table 7.2 Summary of dSph observations by each experiment used in this work. A ‘-’ indicates the experiment did not observe the dSph for this study. For Fermi-LAT, the exposure at 1 GeV is given. For HAWC, $|\Delta\theta|$ is the absolute difference between the source declination and HAWC latitude. HAWC is more sensitive to sources with smaller $|\Delta\theta|$. For IACTs, we show the zenith angle range, the total exposure, the energy range, the angular radius θ of the signal or ON region, the ratio of exposures between the background-control (OFF) and signal (ON) regions (τ), and the significance of gamma-ray excess in standard deviations, σ .

Source name	Fermi-LAT	HAWC	H.E.S.S, MAGIC, VERITAS						
	Exposure (10^{11} s m 2)	$ \Delta\theta $ ($^\circ$)	IACT	Zenith ($^\circ$)	Exposure (h)	Energy range (GeV)	θ ($^\circ$)	τ	S (σ)
Boötes I	2.6	4.5	VERITAS	15 – 30	14.0	100–41000	0.10	8.6	-1.0
Canes Venatici I	2.9	14.6	–	–	–	–	–	–	–
Canes Venatici II	2.9	15.3	–	–	–	–	–	–	–
Carina	3.1	–	H.E.S.S.	27 – 46	23.7	310 – 70000	0.10	18.0	-0.3
Coma Berenices	2.7	4.9	H.E.S.S.	47 – 49	11.4	550 – 70000	0.10	14.4	-0.4
			MAGIC	5 – 37	49.5	60 – 10000	0.17	1.0	–
			MAGIC	29 – 45	52.1	70 – 10000	0.22	1.0	–
Draco	3.8	38.1	VERITAS	25 – 40	49.8	120 – 70000	0.10	9.0	-1.0
Fornax	2.7	–	H.E.S.S.	11 – 25	6.8	230 – 70000	0.10	45.5	-1.5
Hercules	2.8	6.3	–	–	–	–	–	–	–
Leo I	2.5	6.7	–	–	–	–	–	–	–
Leo II	2.6	3.1	–	–	–	–	–	–	–
Leo IV	2.4	19.5	–	–	–	–	–	–	–
Leo V	2.4	–	–	–	–	–	–	–	–
Leo T	2.6	–	–	–	–	–	–	–	–
Sculptor	2.7	–	H.E.S.S.	10 – 46	11.8	200 – 70000	0.10	19.8	-2.2
Segue I	2.5	2.9	MAGIC	13 – 37	158.0	60 – 10000	0.12	1.0	-0.5
			VERITAS	15 – 35	92.0	80 – 50000	0.10	7.6	0.7
Segue II	2.7	–	–	–	–	–	–	–	–
Sextans	2.4	20.6	–	–	–	–	–	–	–
Ursa Major I	3.4	32.9	–	–	–	–	–	–	–
Ursa Major II	4.0	44.1	MAGIC	35 – 45	94.8	120 – 10000	0.30	1.0	-2.1
Ursa Minor	4.1	–	VERITAS	35 – 45	60.4	160 – 93000	0.10	8.4	-0.1

699 calculate the likelihood of each source and model, assuming events are Poisson distributed, with

$$\mathcal{L} = \prod_i \frac{(B_i + S_i)^{N_i} e^{-(B_i + S_i)}}{N_i!} \quad (7.3)$$

700 S_i is the sum of expected number of signal counts. B_i is the number of background counts
 701 observed. N_i is the total number of counts. The i th bin is iterated over spatial and f_{hit} . Then we
 702 combine the profiles across all five experiments. The profile likelihood ratio λ as a function of
 703 annihilation cross-section $\langle\sigma v\rangle$ is computed by:

$$\lambda(\langle\sigma v\rangle | \mathcal{D}_{\text{dSphs}}) = \frac{\mathcal{L}(\langle\sigma v\rangle; \hat{\nu} | \mathcal{D}_{\text{dSphs}})}{\mathcal{L}(\widehat{\langle\sigma v\rangle}; \hat{\nu} | \mathcal{D}_{\text{dSphs}})} \quad (7.4)$$

704 for a considered annihilation channel and DM mass.

705 **TODO: Section pasted from paper. Rephrase cause plagiarism is a thing.** As mentioned pre-
 706 viously, each experiment computes the \mathcal{L}_{lk} from Equation (7.4) differently. The remainder of
 707 this section highlights the differences in this calculation across the experiments. Four experiments,
 708 namely *Fermi*-LAT, H.E.S.S., HAWC and MAGIC, use a binned likelihood to compute the \mathcal{L}_{lk} . For
 709 these experiments, for each observation \mathcal{D}_{lk} of a given dSph l carried out using a given gamma-ray
 710 detector k , the binned likelihood function is:

$$\mathcal{L}_{lk}(\langle\sigma v\rangle; J_l, \nu_{lk} | \mathcal{D}_{lk}) = \prod_{i=1}^{N_E} \prod_{j=1}^{N_P} \left[\mathcal{P}(s_{lk,ij}(\langle\sigma v\rangle, J_l, \nu_{lk}) + b_{lk,ij}(\nu_{lk}) | N_{lk,ij}) \right] \times \mathcal{L}_{lk,\nu}(\nu_{lk} | \mathcal{D}_{\nu_{lk}}) \quad (7.5)$$

711 where N_E and N_P are the number of considered bins in reconstructed energy and arrival
 712 direction, respectively; \mathcal{P} represents a Poisson PDF for the number of gamma-ray candidate events
 713 $N_{lk,ij}$ observed in the i -th bin in energy and j -th bin in arrival direction, when the expected number
 714 is the sum of the expected mean number of signal events s_{ij} (produced by DM annihilation) and of
 715 background events b_{ij} ; $\mathcal{L}_{lk,\nu}$ is the likelihood term for the extra ν_{lk} nuisance parameters that vary
 716 from one instrument k to another. The expected counts for signal events s_{ij} for a given dSph l and
 717 detector k is given by:

$$s_{ij}(\langle\sigma v\rangle, J) = \int_{E'_{\min,i}}^{E'_{\max,i}} dE' \int_{P'_{\min,j}}^{P'_{\max,j}} d\Omega' \int_0^\infty dE \int_{\Delta\Omega_{tot}} d\Omega \int_0^{T_{\text{obs}}} dt \frac{d^2\Phi(\langle\sigma v\rangle, J)}{dEd\Omega} \text{IRF}(E', P' | E, P, t) \quad (7.6)$$

718 where E' and E are the reconstructed and true energies, P' and P the reconstructed and true
 719 arrival directions; $E'_{\min,i}$, $P'_{\min,j}$, $E'_{\max,i}$, and $P'_{\max,j}$ are their lower and upper limits of the i -th
 720 energy bin and the j -th arrival direction bin; T_{obs} is the (dead-time corrected) total observation
 721 time; t is the time along the observations; $d^2\Phi/dEd\Omega$ is the DM flux in the source region (see
 722 Equation (7.1)); and $\text{IRF}(E', P' | E, P, t)$ is the IRF, which can be factorized as the product of the
 723 effective collection area of the detector $A_{\text{eff}}(E, P, t)$, the PDFs for the energy estimator $f_E(E' | E, t)$,
 724 and arrival direction $f_P(P' | E, P, t)$ estimators. Note that for Fermi-LAT, HAWC, MAGIC, and
 725 VERITAS the effect of the finite angular resolution is taken into account through the convolution
 726 of $d\Phi/dEd\Omega$ with f_P in Equation (7.6), whereas in the cases of H.E.S.S. f_P is approximated by a
 727 delta function. This approximation has been made in order to maintain compatibility of the result
 728 with what has been previously published. The difference introduced by this approximation is $< 5\%$
 729 for all considered dSphs. **TODO: End of paper section**

730 From Equation (7.4), we can compute the test statistic (TS) with the ratio test:

$$\text{TS} = -2 \ln \left(\frac{\mathcal{L}}{\mathcal{L}^{\text{max}}} \right). \quad (7.7)$$

731 \mathcal{L}^{max} here is equivalent to $\mathcal{L}(N_i, B_i, S_i = 0)$ or no signal counts.

732 7.4 HAWC Results

733 13 of the 20 dSphs considered for the Glory Duck analysis are within HAWC's field of view.
 734 These dSph are analyzed for DM content according to the likelihood method described in Sec-
 735 tion 7.3.3. The 13 likelihood profiles are then combined to create a combined limit on the dark
 736 matter cross-section. This combination is done for 7 of the 8 annihilation channels used in the Glory
 737 Duck analysis. Figure 7.4 shows the combined limit for all annihilation channels with HAWC only
 738 observations. We also perform 300 studies of Poisson trials on the background. These trials are
 739 used to produce HAWC Brazil bands are shared with the other collaborators for combined Brazil

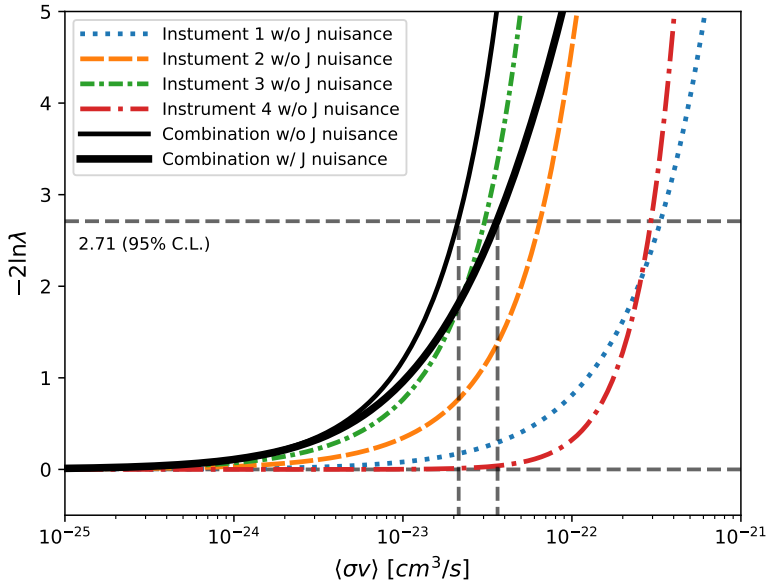


Figure 7.3 Illustration of the combination technique showing a comparison between $-2 \ln \lambda$ provided by four instruments (colored lines) from the observation of the same dSph without any J nuisance and their sum, *i.e.* the resulting combined likelihood (thin black line). According to the test statistics of Equation (7.7), the intersection of the likelihood profiles with the line $-2 \ln \lambda = 2.71$ indicates the 95% C.L. upper limit on $\langle \sigma v \rangle$. The combined likelihood (thin black line) shows a smaller value of upper limit on $\langle \sigma v \rangle$ than those derived by individual instruments. We also show the uncertainties on the J -factor affects the combined likelihood and degrade the upper limit on $\langle \sigma v \rangle$ (thick black line). All likelihood profiles are normalized so that the global minimum $\widehat{\langle \sigma v \rangle}$ is 0. We note that each profile depends on the observational conditions in which a target object was observed. The sensitivity of a given instrument can be degraded and the upper limits less constraining if the observations are performed in non optimal conditions such as a high zenith angle or a short exposure time.

740 Bands. The results on fitting to HAWC's poisson trials of the DM hypothesis is shown in Figure 7.5
 741 for seven of the DM annihilation channels.

742 No DM was found in HAWC observations. The limits are dominated by the dSph Segue1 and
 743 Coma Berenices. The remaining 11 dSphs do no contribute significantly to the limit. Even though
 744 the remaining dSphs have large J -factors, they are towards the edge of HAWC's field of view where
 745 this analysis is less sensitive.

746 7.5 Glory Duck Combined Results

747 The crux of this analysis is that HAWC's results are combined with 4 other gamma-ray obser-
 748 vatories: Fermi-LAT, H.E.S.S., MAGIC, and VERITAS. The complete joint likelihood for the l -th

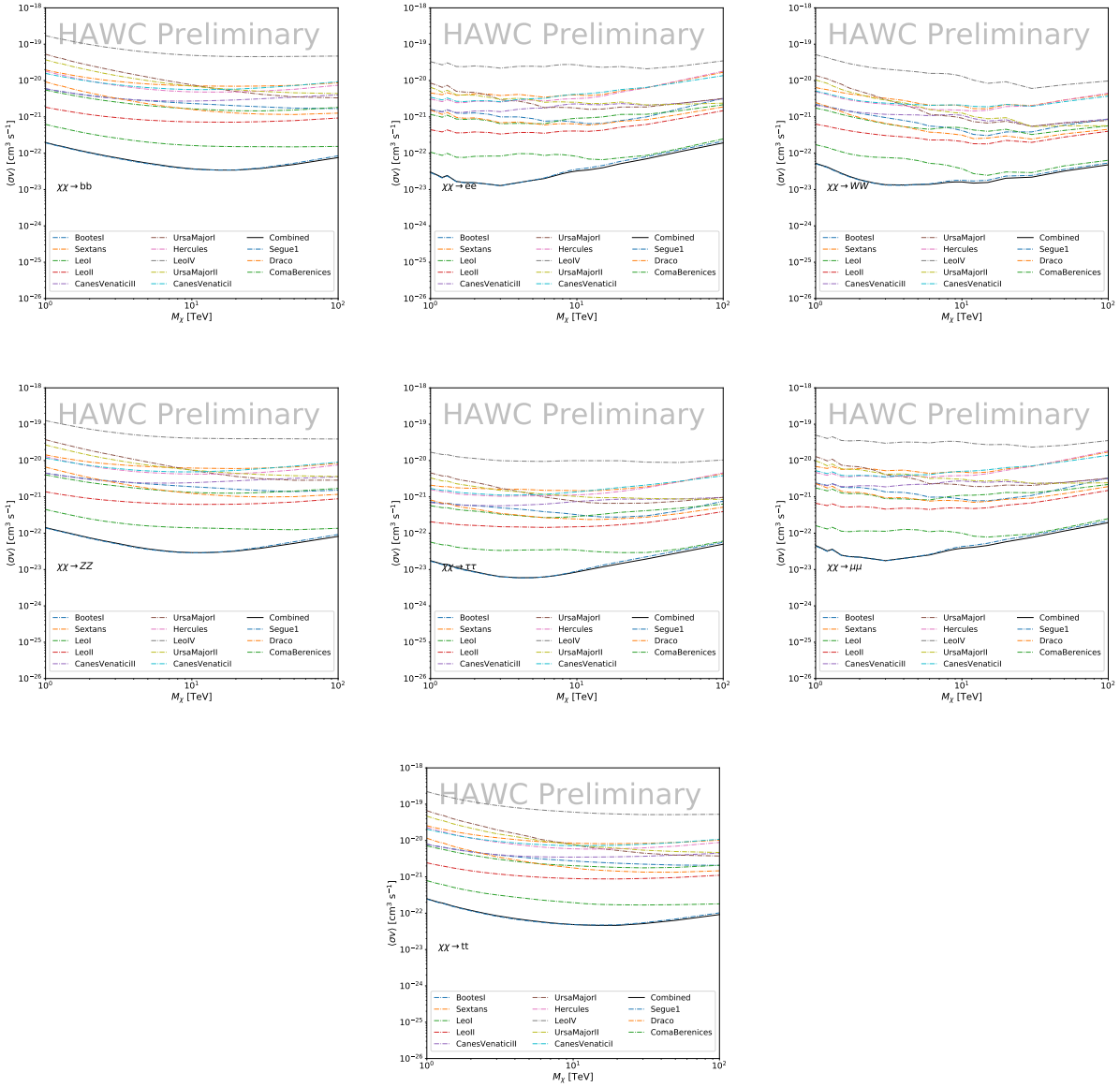


Figure 7.4 HAWC upper limits at 95% confidence level on $\langle\sigma v\rangle$ versus DM mass for seven annihilation channels, using the set of J -factors from Ref. [47] The solid line represents the observed combined limit. Dashed lines represent limits from individual dSphs.

749 dSph is the product of likelihood functions of the 5 experiments.

750 TODO: place holder for results

751 No significant DM emission was observed by any of the five telescopes. We present upper
752 limits on $\langle\sigma v\rangle$ using the test statistics, Eq. (7.7).

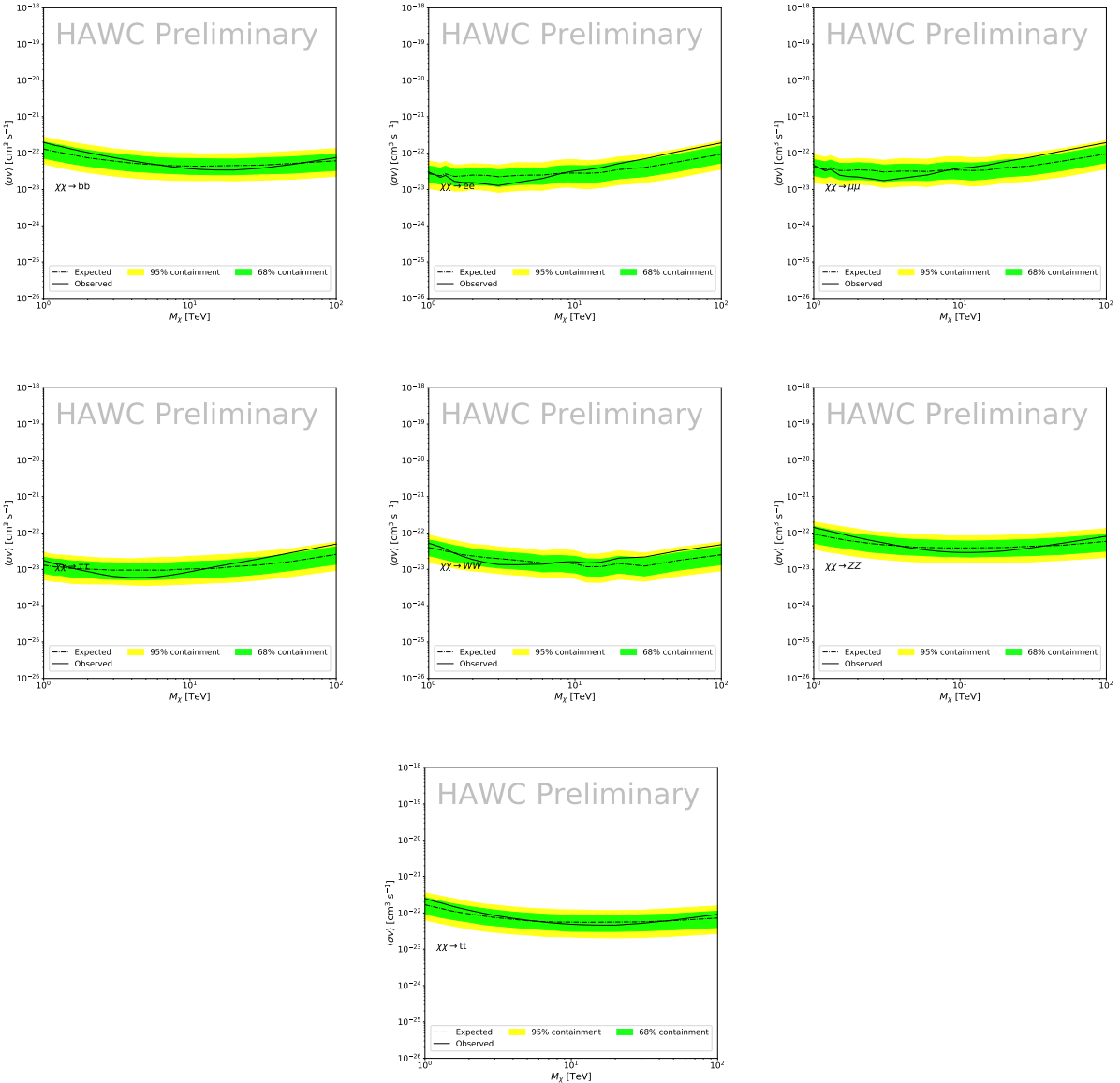


Figure 7.5 HAWC Brazil bands at 95% confidence level on $\langle\sigma v\rangle$ versus DM mass for seven annihilation channels with J -factors from \mathcal{GS} [47]. The solid line represents the combined limit from 13 dSphs. The dashed line is the expected limit. The green band is the 68% containment. The yellow band is the 95% containment.

$$TS = -2 \ln \lambda(\langle\sigma v\rangle), \quad (7.8)$$

753 No significant DM emission was observed by any of the five instruments. We present the upper
 754 limits on $\langle\sigma v\rangle$ assuming seven independent DM self annihilation channels, namely W^+W^- , Z^+Z^- ,
 755 $b\bar{b}$, $t\bar{t}$, e^+e^- , $\mu^+\mu^-$, and $\tau^+\tau^-$. The 68% and 95% containment bands are produced from 300

756 Poisson realizations of the null hypothesis corresponding to each of the combined datasets. These
757 300 realizations are combined identically to dSph observations. The containment bands and the
758 median are extracted from the distribution of resulting limits on the null hypothesis. These 300
759 realizations are obtained either by fast simulations of the OFF observations, for H.E.S.S., MAGIC,
760 VERITAS, and HAWC, or taken from real observations of empty fields of view in the case of
761 Fermi-LAT [48, 49, 50].

762 The obtained limits are shown in Figure 7.6 for the \mathcal{GS} set of J -factors [47] and in Figure 7.7
763 for the \mathcal{B} set of J -factors [46, 51]. The combined limits are presented with their 68% and 95%
764 containment bands, and are expected to be close to the median limit when no signal is present.
765 We observe agreement with the null hypothesis for all channels, within 2σ standard deviations,
766 between the observed limits and the expectations given by the median limits. Limits obtained from
767 each detector are also indicated in the figures, where limits for all dSphs observed by the specific
768 instrument have been combined.

769 Below ~ 300 GeV, the *Fermi*-LAT dominates the DM limits for all annihilation channels. From
770 ~ 300 GeV to ~ 2 TeV, *Fermi*-LAT continues to dominate for the hadronic and bosonic DM channels,
771 yet the IACTs (H.E.S.S., MAGIC, and VERITAS) and *Fermi*-LAT all contribute to the limit for
772 leptonic DM channels. For DM masses between ~ 2 TeV to ~ 10 TeV, the IACTs dominate leptonic
773 DM annihilation channels, whereas both the *Fermi*-LAT and the IACTs dominate bosonic and
774 hadronic DM annihilation channels. From ~ 10 TeV to ~ 100 TeV, both the IACTs and HAWC
775 contribute significantly to the leptonic DM limit. For hadronic and bosonic DM, the IACTs and
776 *Fermi*-LAT both contribute strongly.

777 We notice that the limits computed using the \mathcal{B} set of J -factor are always better compared to the
778 ones calculated with the \mathcal{GS} set. For the W^+W^- , Z^+Z^- , $b\bar{b}$, and $t\bar{t}$ channels, the ratio between the
779 limits computed with the two sets of J -factor is varying between a factor of ~ 3 and ~ 5 depending
780 on the energy, with the largest ratio around 10 TeV. For the channels e^+e^- , $\mu^+\mu^-$, and $\tau^+\tau^-$, the
781 ratio lies between ~ 2 to ~ 6 , being maximum around 1 TeV. Examining Figure 7.12 and Figure 7.13
782 in Section 7.7, these differences are explained by the fact that the \mathcal{B} set provides higher J -factors

783 for the majority of the studied dSphs, with the notable exception of Segue I. The variation on the
784 ratio of the limits for the two sets is due to different dSph dominating the limits depending on the
785 energy. This pushes the range of thermal cross-section which can be excluded to higher mass. This
786 comparison demonstrates the magnitude of systematic uncertainties associated with the choice of
787 the J -factor

788 This comparison demonstrates the magnitude of systematic uncertainties associated with the
789 choice of the J -factor calculation. The \mathcal{GS} and \mathcal{B} sets present a difference in the limits for all
790 channels of about This difference is explained, see Figure 7.12 and Figure 7.13 in Appendix, by the
791 fact that the \mathcal{B} set provides higher J factors for all dSph except for Segue I. This pushes the range
792 of thermal cross-section which can be excluded to higher mass.

793 7.6 Appendix: HAWC Systematics

794 7.6.1 Inverse Compton Scattering

795 The DM-DM annihilation channels produce many high energy electrons regardless of the
796 primary annihilation channel. These high energy electrons can produce high energy gamma-rays
797 through Inverse Compton Scattering (ICS). If this effect is strong, it would change the morphology
798 of the source and increase the total expected gamma-ray counts from any source. The PPPC [43]
799 provides tools in Mathematica for calculating the impact of ICS for an arbitrary location in the
800 sky for a specified annihilation channel. We calculated the change in gamma-ray counts for DM
801 annihilation to primary $e\bar{e}$ for RA and Dec corresponding to Segue1 and Coma Berenices. These
802 dSphs were chosen because they are the strongest contributors to the limit. $e\bar{e}$ was selected because
803 it would have the largest number of high energy electrons. The effect was found to be on the order
804 of 10^{-7} on the gamma-ray spectrum. As a result, this systematic is not considered in our analysis.

805 7.6.2 Point Source Versus Extended Source Limits

806 The previous DM search toward dSph approximated the dSphs as point sources [45]. In
807 this analysis, the dSphs are implemented as extended with J-factor distributions following those
808 produced by [47]. The resolution of the cited map is much finer than HAWC's angular resolution.

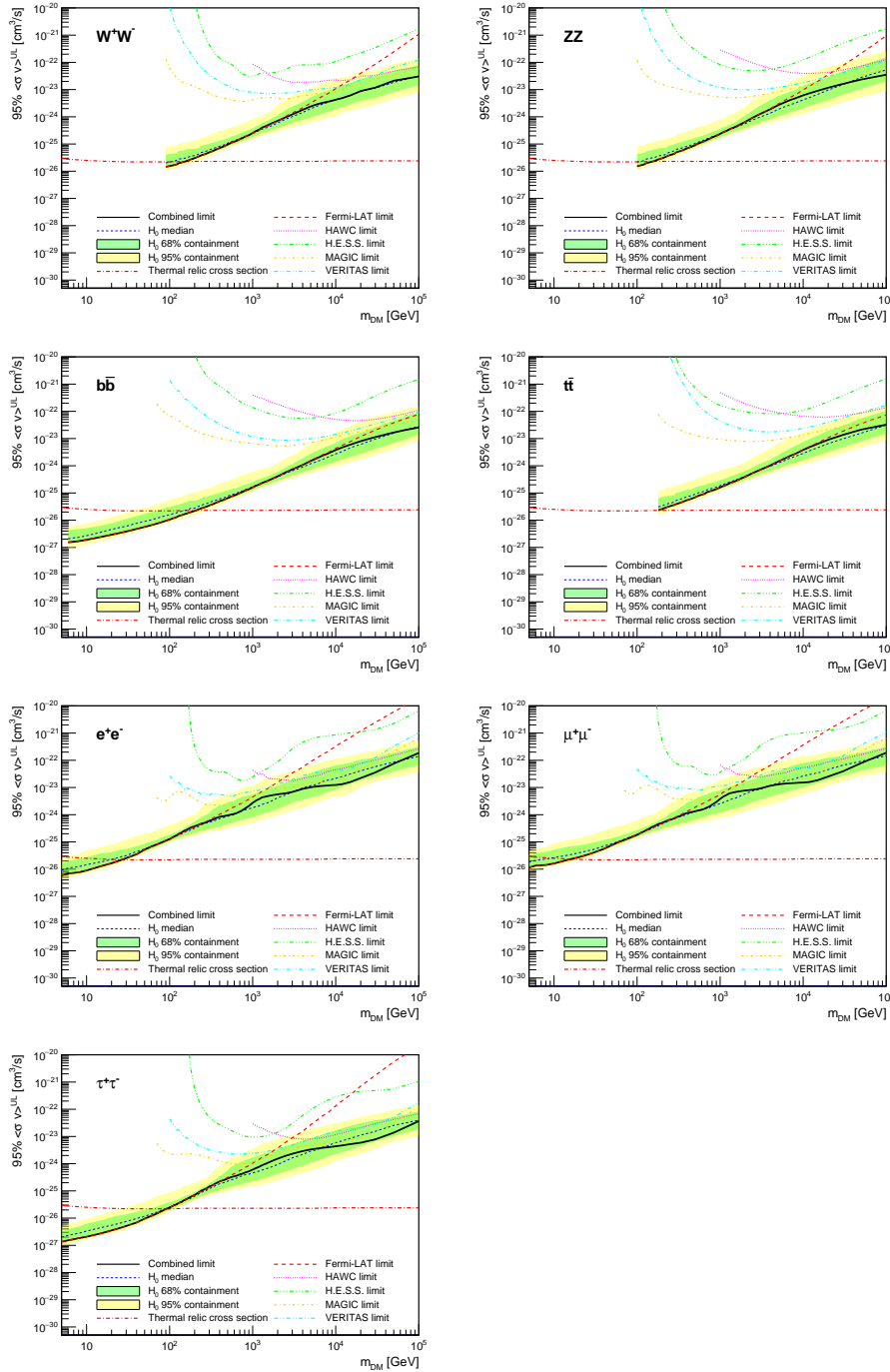


Figure 7.6 Upper limits at 95% confidence level on $\langle\sigma v\rangle$ in function of the DM mass for eight annihilation channels, using the set of J factors from Ref. [47] (\mathcal{GS} set in Table 7.1). The black solid line represents the observed combined limit, the black dashed line is the median of the null hypothesis corresponding to the expected limit, while the green and yellow bands show the 68% and 95% containment bands. Combined upper limits for each individual detector are also indicated as solid, colored lines. The value of the thermal relic cross-section in function of the DM mass is given as the red dotted-dashed line [52].

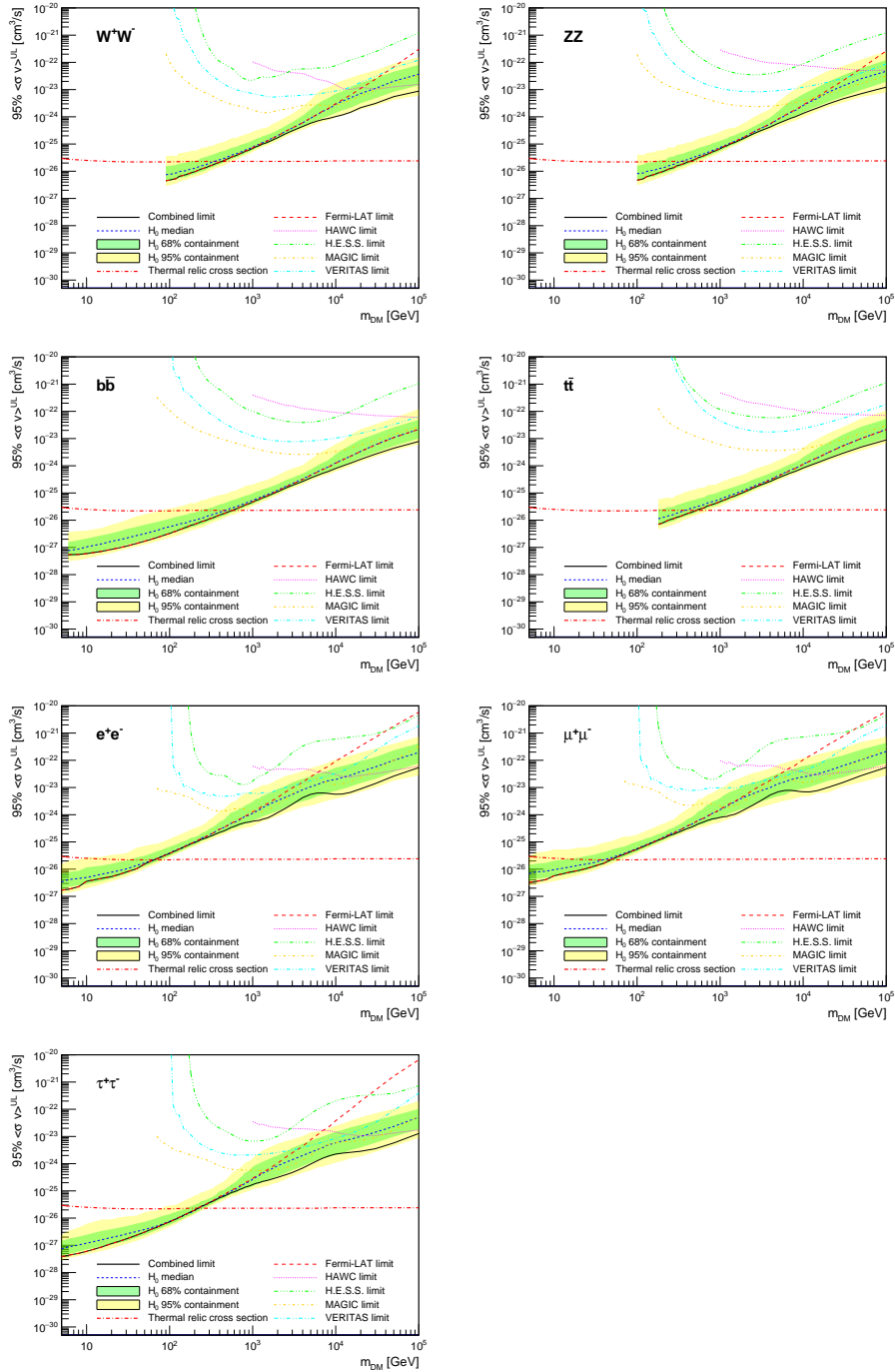


Figure 7.7 Same as Fig. 7.6, using the set of J factors from Ref. [46, 51] (\mathcal{B} set in Table 7.1).

809 The vast majority of the J-factor distribution is represented on the central HAWC pixel of the dSph
810 spatial map. However, the neighboring 8 pixels are not negligible and contribute to our limit.

811 Figure 7.9 shows a substantial improvement to the limit for Segue1. Fig. 7.10 however showed
812 identical limits. These disparities are best explained by the relative difference in their J-Factors.

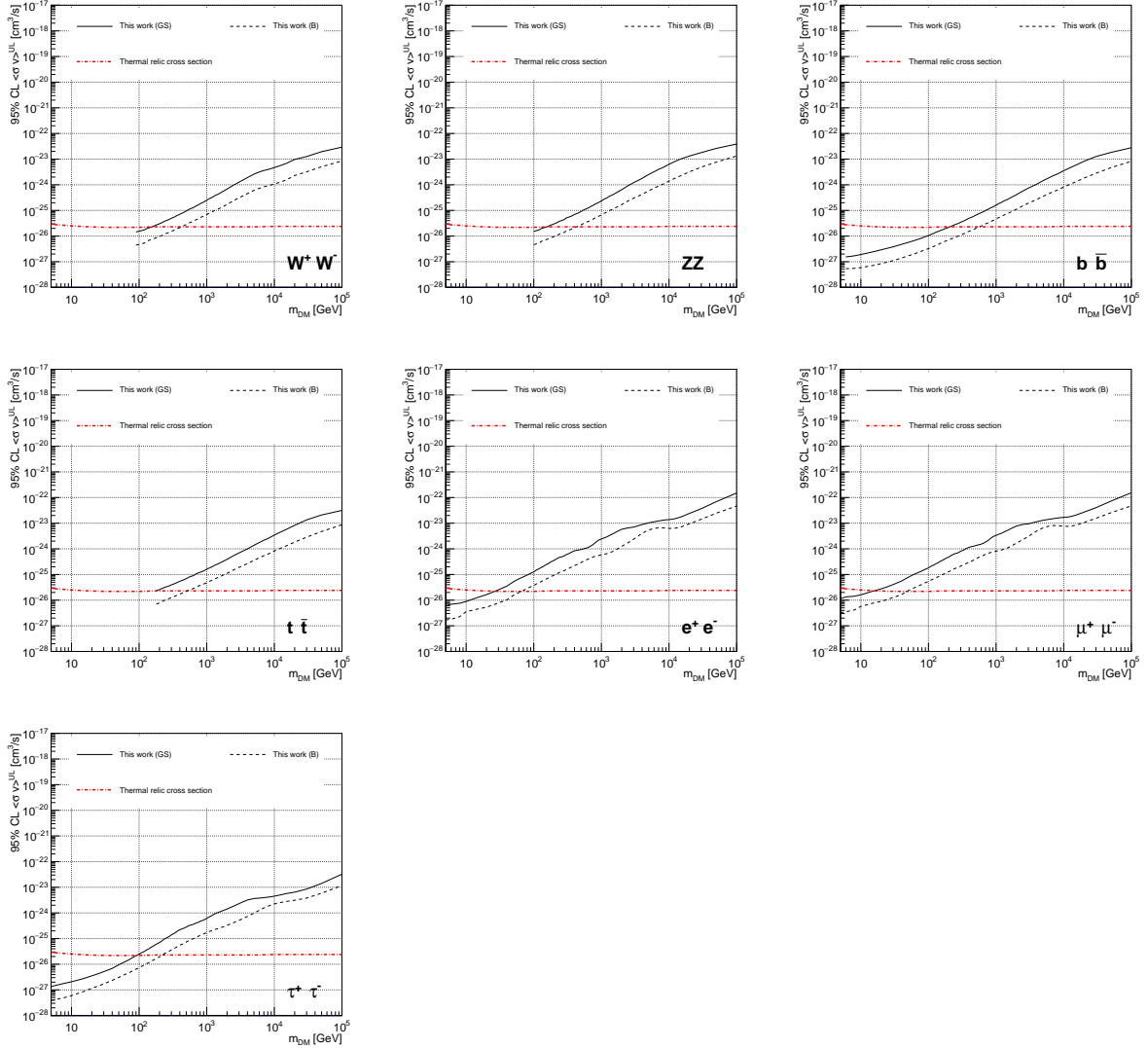


Figure 7.8 Comparisons of the combined limits at 95% confidence level for each of the eight annihilation channels when using the J factors from Ref. [47] (\mathcal{GS} set in Table 7.1), plain lines, and the J factor from Ref. [46, 51] (\mathcal{B} set in Table 7.1), dashed lines. The cross-section given by the thermal relic is also indicated [52].

813 Both dSphs pass almost overhead the HAWC detector, however Segue1 has the larger J-Factor
 814 between the two. Adjacent pixels to the central pixel will therefore contribute to the limits. This is
 815 the case for other dSph that are closer to overhead the HAWC detector.
 816 Comparison plots for all sources and the combined limit can be found in the sandbox for the
 817 Glory Duck project.

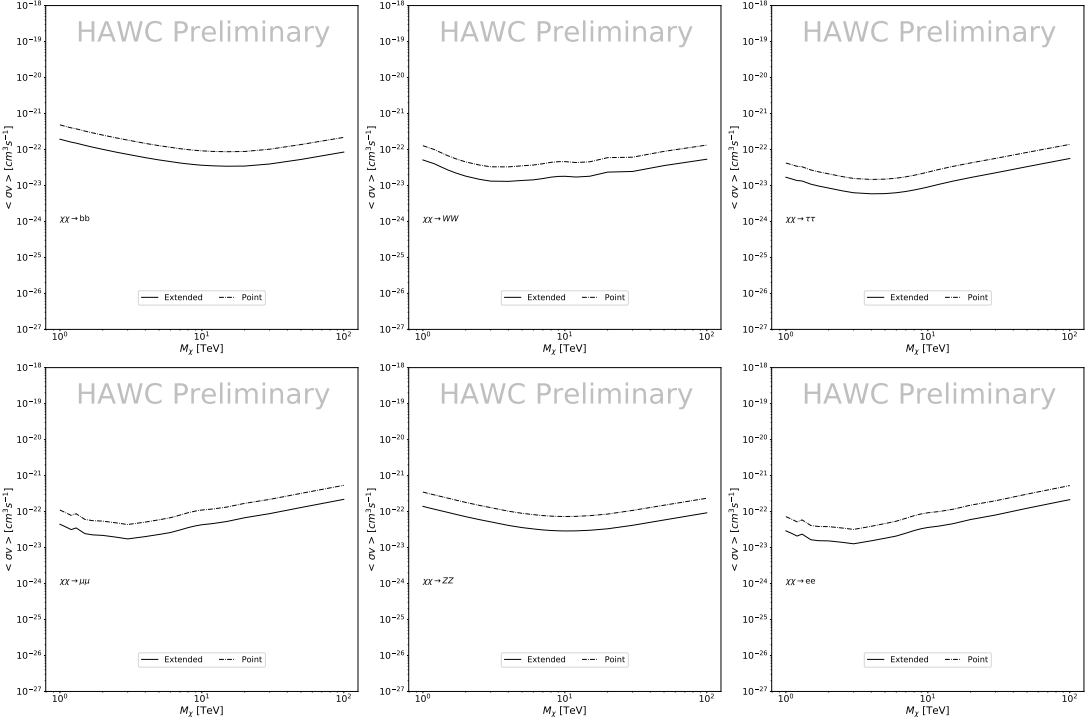


Figure 7.9 Comparisons of the combined limits at 95% confidence level for a point source analysis and extended source using [47] *GS* J-factor distributions and PPPC [43] annihilation spectra. Shown are the limits for Segue1 which will have the most significant impact on the combined limit. 6 of the 7 DM annihilation channels are shown. Solid lines are extended source studies. Dashed lines are point source studies. Overall, the extended source analysis improves the limit by a factor of 2.

818 7.6.3 Impact of Pointing Systematic

819 During the analysis it was discovered that reconstruction of gamma-rays. Slides describing this
 820 systematic can be found [here](#). Shown on the presentation is dependence on the pointing systematic
 821 on declination. New spatial profiles were generated for every dSph and limits were computed for
 822 the adjusted declination.

823 Section 7.6.3 demonstrates the impact of this systematic for all DM annihilation channels
 824 studied by HAWC. The impact is a tiny improvement, yet mostly identical, to the combined limits.

825 7.7 J-factor distributions

826 We show in this appendix a comparison between the *J*-factors computed by Geringer-Sameth
 827 *et al.* [47] (the *GS* set) and the ones computed by Bonnivard *et al.* [46, 51] (the *B* set). The
 828 *GS* *J*-factors are computed through a Jeans analysis of the kinematic stellar data of the selected

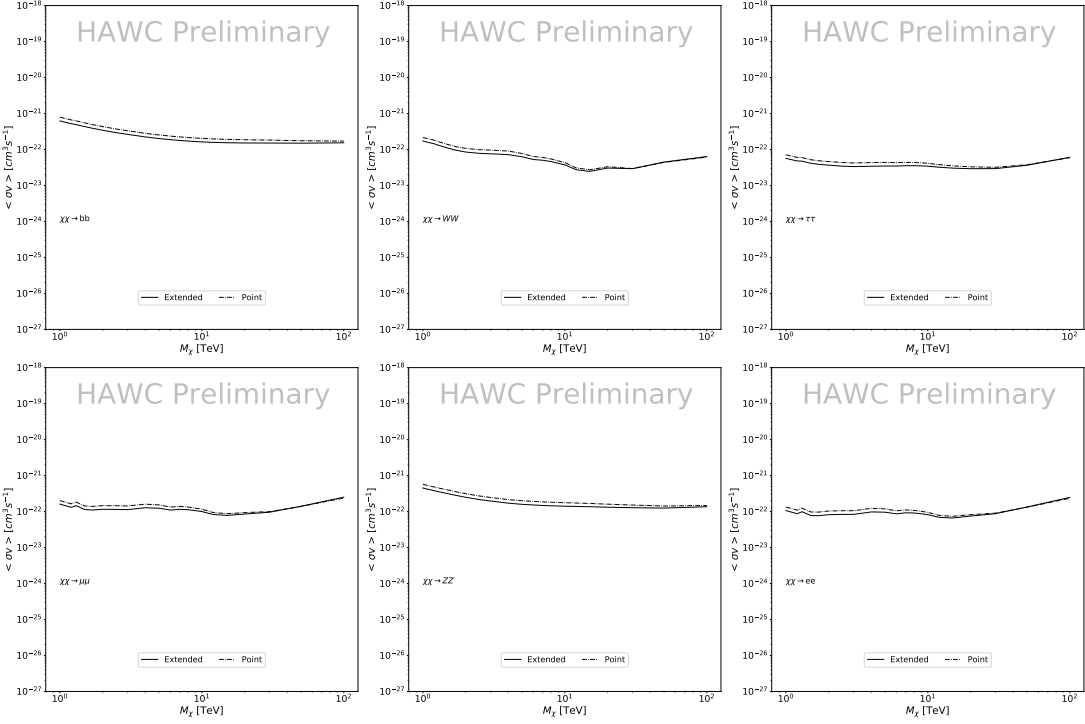


Figure 7.10 Same as Fig. 7.9 on Coma Berenices. This dSph also contributes significantly to the limit. The limits are identical in this case.

829 dSphs, assuming a dynamic equilibrium and a spherical symmetry for the dSphs. They adopted
 830 the generalized DM density distribution, known as Zhao-Hernquist, introduced by [53], carrying
 831 three additional index parameters to describe the inner and outer slopes, and the break of the
 832 density profile. Such a profile parametrization allows the reduction of the theoretical bias from
 833 the choice of a specific radial dependency on the kinematic data. In other words, the increase of
 834 free parameters with the use of the Zhao-Hernquist profile allows a better description of the mass
 835 density distribution of dark matter.

836 In addition, a constant velocity anisotropy profile and a Plummer light profile [54] for the stellar
 837 distribution were assumed. The velocity anisotropy profile depends on the radial and tangential
 838 velocity dispersions. However, its determination remains challenging since only the line-of-sight
 839 velocity dispersion can be derived from velocity measurements. Therefore, the parametrization of
 840 the anisotropy profile is obtained from simulated halos (see [55] for more details). They provide the
 841 values of the J -factors of regions extending to various angular radius up to the outermost member
 842 star.

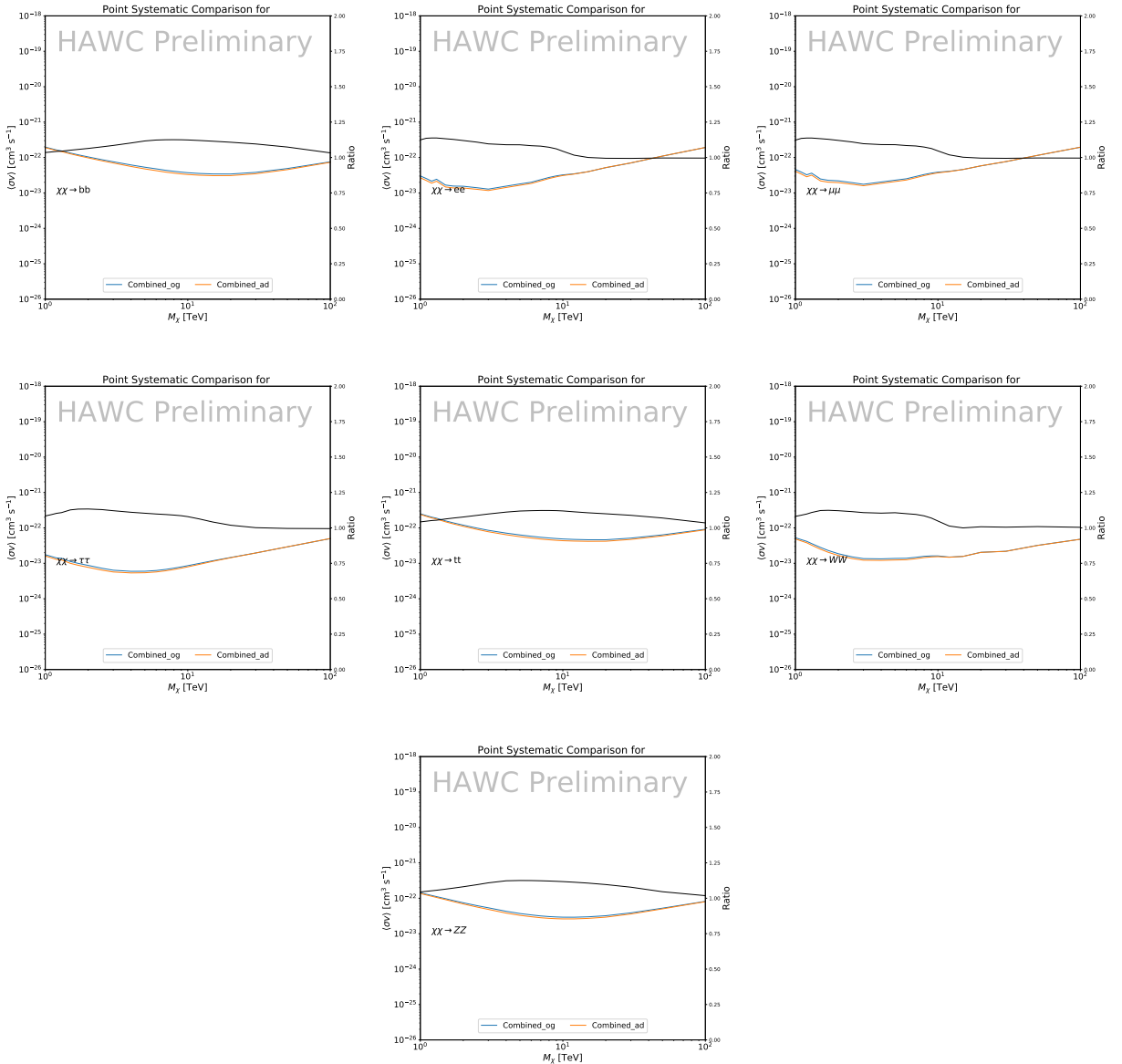


Figure 7.11 Comparison of combined limits when correcting for HAWC's pointing systematic. All DM annihilation channels are shown. The solid black line is the ratio between published limit to the declination corrected limit. The blue solid line or "Combined_og" represented the limits computed for Glory Duck. The solid orange line or "Combined_ad" represented the limits computed after correcting for the pointing systematic.

843 The \mathcal{B} J -factors were computed through a Jeans analysis taking into account the systematic
 844 uncertainties induced by the DM profile parametrization, the radial velocity anisotropy profile, and
 845 the triaxiality of the halo of the dwarf galaxies. They performed a more complete study of the dSph
 846 kinematics and dynamics than \mathcal{GS} for the determination of the J -factor. Conservative values of the

847 J -factors where obtained using an Einasto DM density profile [56], a realistic anisotropy profile
848 known as the Baes & Van Hese profile [57] which takes into account that the inner regions can be
849 significantly non-isotropic, and a Zhao-Hernquist light profile [53].

850 For both sets, J -factor values are provided for all dSphs as a function of the radius of the
851 integration region [47, 46, 51]. Table 7.1 shows the heliocentric distance and Galactic coordinates
852 of the twenty dSphs, together with the two sets of J -factor values integrated up to the outermost
853 observed star for \mathcal{GS} and the tidal radius for \mathcal{B} . Both J -factor sets were derived through a Jeans
854 analysis based on the same kinematic data, except for Draco where the measurements of [58] have
855 been adopted in the computation of the \mathcal{B} value. The computations for producing the \mathcal{GS} and \mathcal{B}
856 samples differ in the choice of the DM density, velocity anisotropy, and light profiles, for which the
857 set \mathcal{B} takes into account some sources of systematic uncertainties.

858 Figure 7.12 and Figure 7.13 show the comparisons for the J -factor versus the angular radius
859 for each of the 20 dSphs used in this study. The uncertainties provided by the authors are also
860 indicated in the figures. For the \mathcal{GS} set, the computation stops at the angular radius corresponding
861 to the outermost observed star, while for the \mathcal{B} set, the computation stops at the angular radius
862 corresponding to the tidal radius.

863 7.8 Discussion and Conclusions

864 In this multi-instrument analysis, we have used observations of 20 dSphs from the gamma-ray
865 telescopes Fermi-LAT, H.E.S.S., MAGIC, VERITAS, and HAWC to perform a collective DM
866 search annihilation signals. The data were combined across sources and detectors to significantly
867 increase the sensitivity of the search. We have observed no significant deviation from the null, no
868 DM hypothesis, and so present our results in terms of upper limits on the annihilation cross section
869 for seven potential DM annihilation channels.

870 Fermi-LAT brings the most stringent constraints for continuum channels below approximately
871 1 TeV. the remaining detectors dominate at higher energies. Overall, for multi-TeV DM mass,
872 the combined DM constraints from all five telescopes are 2-3 times stronger than any individual
873 telescope for multi-TeV DM.

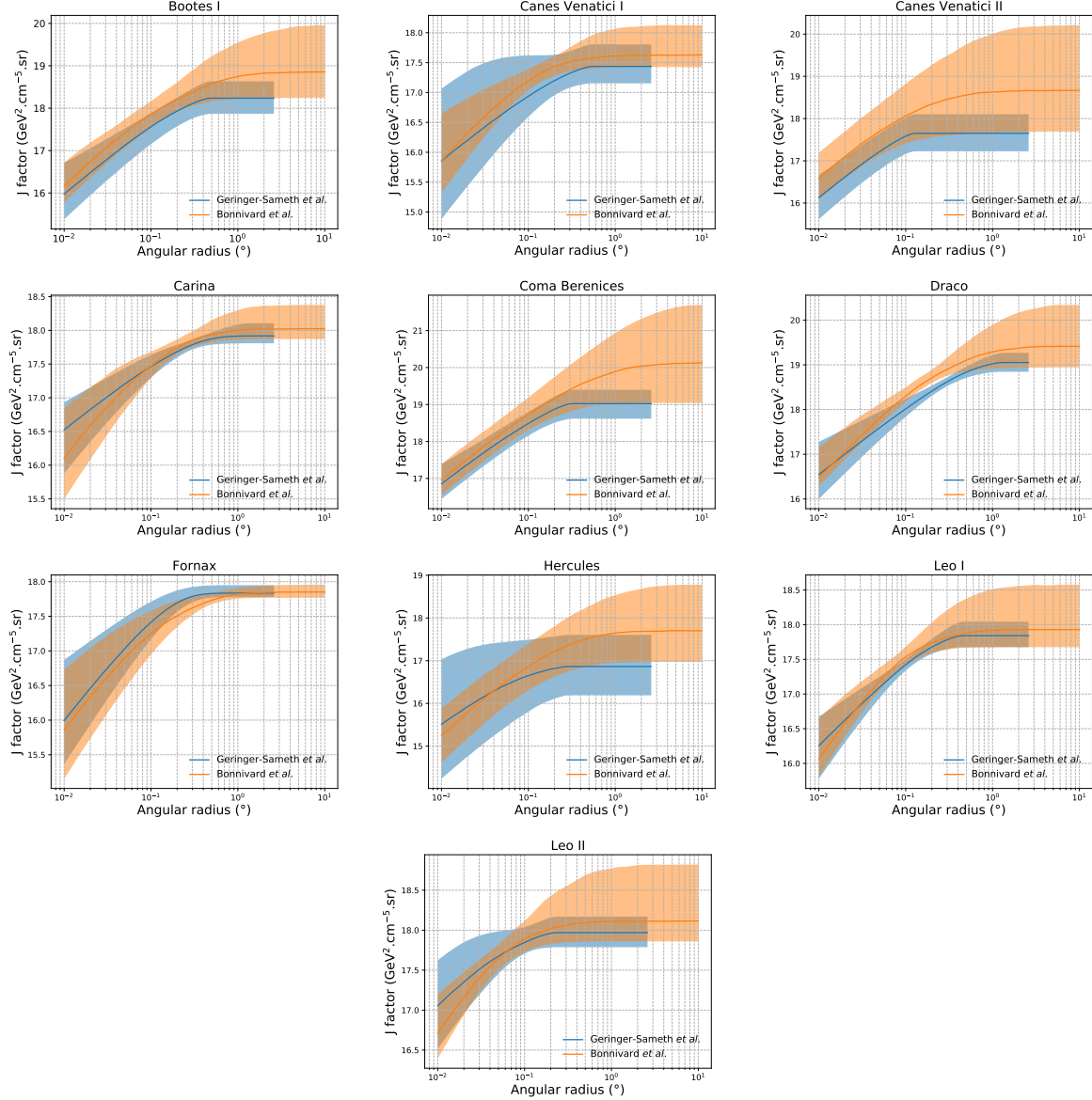


Figure 7.12 Comparisons between the J -factors versus the angular radius for the computation of J factors from Ref. [47] (\mathcal{GS} set in Table 7.1) in blue and for the computation from Ref. [46, 51] (\mathcal{B} set in Tab. 7.1) in orange. The solid lines represent the central value of the J -factors while the shaded regions correspond to the 1σ standard deviation.

874 Derived from observations of many dSphs, our results produce robust limits given the DM
 875 content of the dSphs is relatively well constrained. The obtained limits span the largest mass
 876 range of any WIMP DM search. Our combined analysis improves the sensitivity over previously
 877 published results from each detectors which produces the most stringent limits on DM annihilation
 878 from dSphs. These results are based on deep exposures of the most promising known dSphs with

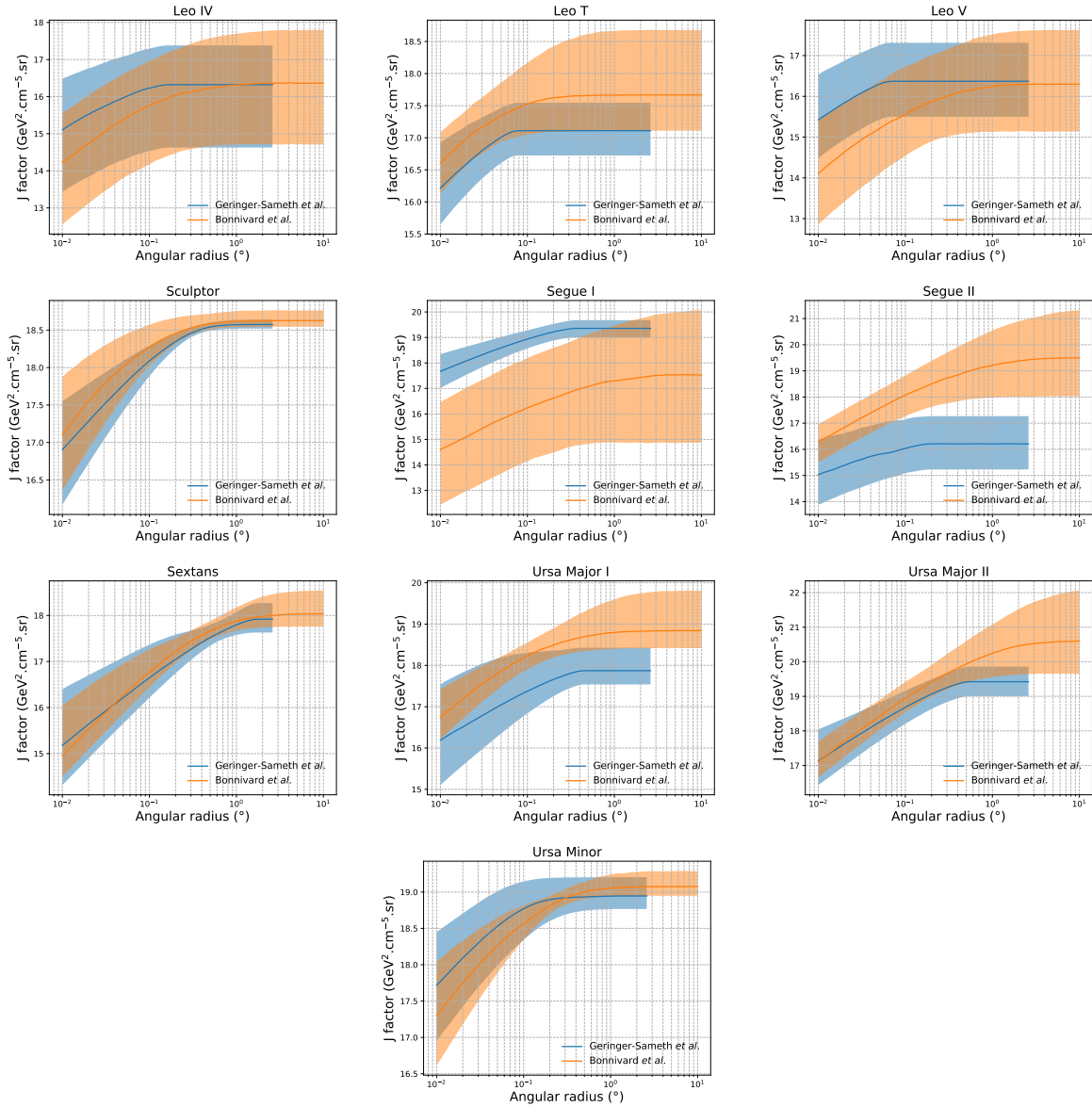


Figure 7.13 Comparisons between the J -factors versus the angular radius for the computation of J factors from Ref. [47] (\mathcal{GS} set in Tab. 7.1) in blue and for the computation from Ref. [46, 51] (\mathcal{B} set in Tab. 7.1) in orange. The solid lines represent the central value of the J -factors while the shaded regions correspond to the 1σ standard deviation.

879 the currently most sensitive gamma-ray instruments. Therefore, our results constitute a legacy of
 880 a generation of gamma-ray instruments on WIMP DM searches towards dSphs. Our results will
 881 remain the reference in the field until a new generation of more sensitive gamma-ray instruments
 882 begin operations, or until new dSphs with higher J -factors are discovered.

883 This analysis serves as a proof of concept for future multi-instrument and multi-messenger

884 combination analyses. With this collaborative effort, we have managed to sample over four orders
885 in magnitude in gamma-ray energies with distinct observational techniques. Determining the nature
886 of DM continues to be an elusive and difficult problem. Larger datasets with diverse measurement
887 techniques could be essential to tackling the DM problem. A future collaboration using similar
888 techniques as the ones described in this paper could grow even beyond gamma rays. The models we
889 used for this study include annihilation channels with neutrinos in the final state. Advanced studies
890 could aim to merge our results with those from neutrino observatories with large data sets. Efforts
891 are already underway to add data from the IceCube, ANTARES, and KM3NeT observatories to
892 these gamma-ray results.

893 From this work, a selection of the best candidates for observations, according to the latest
894 knowledge on stellar dynamics and modelling techniques for the derivation of the J -factors on the
895 potential dSphs targets, is highly desirable at the time that new experiments are starting their dark
896 matter programmes using dSphs. Given the systematic uncertainty inherent to the derivation of
897 the J -factors, an informed observational strategy would be to select both objects with the highest
898 J -factors that could lead to DM signal detection, and objects with robust J -factor predictions, i.e.
899 with kinematic measurements on many bright stars, which would strengthen the DM interpretation
900 reliability of the observation outcome.

901 This analysis combines data from multiple telescopes to produce strong constraints on astro-
902 physical objects. From this perspective, these methods can be applied beyond just DM searches.
903 Almost every astrophysical study can benefit from multi-telescope, multi-wavelength gamma-ray
904 studies. We have enabled these telescopes to study the cosmos with greater precision and detail.
905 Many astrophysical searches can benefit from multi-instrument gamma-ray studies, for which our
906 analysis lays the foundation.

CHAPTER 8

NU DUCK

907

CHAPTER 9**MULTITHREADING HAWC ANALYSES FOR DARK MATTER SEARCHES**

BIBLIOGRAPHY

- 910 [1] Anne M. Green. “Dark matter in astrophysics/cosmology”. In: *SciPost Phys. Lect.*
 911 *Notes* (2022), p. 37. doi: [10.21468/SciPostPhysLectNotes.37](https://doi.org/10.21468/SciPostPhysLectNotes.37). URL: <https://scipost.org/10.21468/SciPostPhysLectNotes.37>.
- 913 [2] Bing-Lin Young. “A survey of dark matter and related topics in cosmology”. In: *Frontiers*
 914 *of Physics* 12 (Oct. 2016). doi: <https://doi.org/10.1007/s11467-016-0583-4>.
 915 URL: <https://doi.org/10.1007/s11467-016-0583-4>.
- 916 [3] Gianfranco Bertone, Dan Hooper, and Joseph Silk. “Particle dark matter: evidence,
 917 candidates and constraints”. In: *Physics Reports* 405.5 (2005), pp. 279–390. ISSN:
 918 0370-1573. doi: <https://doi.org/10.1016/j.physrep.2004.08.031>. URL:
 919 <https://www.sciencedirect.com/science/article/pii/S0370157304003515>.
- 920 [4] Gianfranco Bertone and Dan Hooper. “History of dark matter”. In: *Rev. Mod. Phys.*
 921 90 (4 Aug. 2018), p. 045002. doi: [10.1103/RevModPhys.90.045002](https://doi.org/10.1103/RevModPhys.90.045002). URL: <https://link.aps.org/doi/10.1103/RevModPhys.90.045002>.
- 923 [5] Fritz Zwicky. “The Redshift of Extragalactic Nebulae”. In: *Helvetica Physica Acta* 6.
 924 (1933), pp. 110–127. doi: [10.5169/seals-110267](https://doi.org/10.5169/seals-110267).
- 925 [6] Vera C. Rubin and Jr. Ford W. Kent. “Rotation of the Andromeda Nebula from a
 926 Spectroscopic Survey of Emission Regions”. In: *ApJ* 159 (Feb. 1970), p. 379. doi:
 927 [10.1086/150317](https://doi.org/10.1086/150317).
- 928 [7] K. G. Begeman, A. H. Broeils, and R. H. Sanders. “Extended rotation curves of spiral galaxies:
 929 dark haloes and modified dynamics”. In: *Monthly Notices of the Royal Astronomical Society* 249.3 (Apr. 1991), pp. 523–537. ISSN: 0035-8711. doi: [10.1093/mnras/249.3.523](https://doi.org/10.1093/mnras/249.3.523).
 930 eprint: <https://academic.oup.com/mnras/article-pdf/249/3/523/18160929/mnras249-0523.pdf>. URL: <https://doi.org/10.1093/mnras/249.3.523>.
- 933 [8] *Different types of gravitational lenses*. website. Feb. 2004. URL: <https://esahubble.org/images/heic0404b/>.
- 935 [9] Douglas Clowe et al. “A Direct Empirical Proof of the Existence of Dark Matter”. In: *apjl*
 936 648.2 (Sept. 2006), pp. L109–L113. doi: [10.1086/508162](https://doi.org/10.1086/508162). arXiv: [astro-ph/0608407](https://arxiv.org/abs/astro-ph/0608407)
 937 [[astro-ph](#)].
- 938 [10] Planck Collaboration and N. et. al. Aghanim. “Planck 2018 results I. Overview and the
 939 cosmological legacy of Planck”. In: *A&A* 641 (2020). doi: [10.1051/0004-6361/201833880](https://doi.org/10.1051/0004-6361/201833880). URL: <https://doi.org/10.1051/0004-6361/201833880>.
- 941 [11] Wayne Hu. *Matter Density Animation*. web. 2024. URL: <http://background.uchicago.edu/~whu/animbut/anim2.html>.

- 943 [12] Wenlong Yuan et al. “A First Look at Cepheids in a Type Ia Supernova Host with JWST”. in:
944 *The Astrophysical Journal Letters* 940.1 (Nov. 2022). doi: [10.3847/2041-8213/ac9b27](https://doi.org/10.3847/2041-8213/ac9b27).
945 URL: <https://dx.doi.org/10.3847/2041-8213/ac9b27>.
- 946 [13] Wendy L. Freedman. “Measurements of the Hubble Constant: Tensions in Perspective”. In:
947 *The Astrophysical Journal* 919.1 (Sept. 2021), p. 16. doi: [10.3847/1538-4357/ac0e95](https://doi.org/10.3847/1538-4357/ac0e95).
948 URL: <https://dx.doi.org/10.3847/1538-4357/ac0e95>.
- 949 [14] Jodi Cooley. “Dark Matter direct detection of classical WIMPs”. In: *SciPost Phys. Lect.
950 Notes* (2022), p. 55. doi: [10.21468/SciPostPhysLectNotes.55](https://doi.org/10.21468/SciPostPhysLectNotes.55). URL: <https://scipost.org/10.21468/SciPostPhysLectNotes.55>.
- 952 [15] “Search for new phenomena in events with an energetic jet and missing transverse momentum
953 in pp collisions at $\sqrt{s} = 13$ TeV with the ATLAS detector”. In: *Phys. Rev. D* 103
954 (11 July 2021), p. 112006. doi: [10.1103/PhysRevD.103.112006](https://doi.org/10.1103/PhysRevD.103.112006). URL: <https://link.aps.org/doi/10.1103/PhysRevD.103.112006>.
- 956 [16] *Jetting into the dark side: a precision search for dark matter*. website. July 2020. URL:
957 <https://atlas.cern/updates/briefing/precision-search-dark-matter>.
- 958 [17] Celine Armand et. al. “Combined dark matter searches towards dwarf spheroidal galaxies
959 with Fermi-LAT, HAWC, H.E.S.S., MAGIC, and VERITAS”. in: *Proceedings of Science*.
960 Vol. 395. Mar. 2022. doi: <https://doi.org/10.22323/1.395.0528>.
- 961 [18] Tracy R. Slatyer. “Les Houches Lectures on Indirect Detection of Dark Matter”. In: *SciPost
962 Phys. Lect. Notes* (2022), p. 53. doi: [10.21468/SciPostPhysLectNotes.53](https://doi.org/10.21468/SciPostPhysLectNotes.53). URL:
963 <https://scipost.org/10.21468/SciPostPhysLectNotes.53>.
- 964 [19] Christian W Bauer, Nicholas L. Rodd, and Bryan R. Webber. “Dark matter spectra from
965 the electroweak to the Planck scale”. In: *Journal of High Energy Physics* 2021.1029-8479
966 (June 2021). doi: [https://doi.org/10.1007/JHEP06\(2021\)121](https://doi.org/10.1007/JHEP06(2021)121).
- 967 [20] Riccardo Catena and Piero Ullio. “A novel determination of the local dark matter density”.
968 In: *Journal of Cosmology and Astroparticle Physics* 2010.08 (Aug. 2010), p. 004. doi:
969 [10.1088/1475-7516/2010/08/004](https://doi.org/10.1088/1475-7516/2010/08/004). URL: <https://dx.doi.org/10.1088/1475-7516/2010/08/004>.
- 971 [21] B. P. Abbott et al. “Observation of Gravitational Waves from a Binary Black Hole Merger”.
972 In: *Phys. Rev. Lett.* 116 (6 Feb. 2016), p. 061102. doi: [10.1103/PhysRevLett.116.061102](https://doi.org/10.1103/PhysRevLett.116.061102). URL: <https://link.aps.org/doi/10.1103/PhysRevLett.116.061102>.
- 974 [22] R. Abbasi et. al. “Observation of high-energy neutrinos from the Galactic plane”. In: *Science*
975 380.6652 (June 2023), pp. 1338–1343.
- 976 [23] NASA Goddard Space Flight Center. *Fermi’s 12-year view of the gamma-ray sky*. website.

- 977 2022. URL: <https://svs.gsfc.nasa.gov/14090>.
- 978 [24] Marco Cirelli et al. “PPPC 4 DM ID: a poor particle physicist cookbook for dark matter
979 indirect detection”. In: *Journal of Cosmology and Astroparticle Physics* 2011.03 (Mar.
980 2011), p. 051. doi: [10.1088/1475-7516/2011/03/051](https://doi.org/10.1088/1475-7516/2011/03/051). URL: <https://dx.doi.org/10.1088/1475-7516/2011/03/051>.
- 982 [25] W. B. Atwood et al. “The Large Area Telescope on the Fermi Gamma-Ray Space Telescope
983 Mission”. In: *apj* 697.2 (June 2009), pp. 1071–1102. doi: [10.1088/0004-637X/697/2/1071](https://doi.org/10.1088/0004-637X/697/2/1071). arXiv: [0902.1089 \[astro-ph.IM\]](https://arxiv.org/abs/0902.1089).
- 985 [26] M. Ackermann et al. “Searching for Dark Matter Annihilation from Milky Way Dwarf
986 Spheroidal Galaxies with Six Years of Fermi Large Area Telescope Data”. In: *prl* 115.23,
987 231301 (Dec. 2015), p. 231301. doi: [10.1103/PhysRevLett.115.231301](https://doi.org/10.1103/PhysRevLett.115.231301). arXiv:
988 [1503.02641 \[astro-ph.HE\]](https://arxiv.org/abs/1503.02641).
- 989 [27] Mattia Di Mauro, Martin Stref, and Francesca Calore. “Investigating the effect of Milky
990 Way dwarf spheroidal galaxies extension on dark matter searches with Fermi-LAT data”.
991 In: *Phys. Rev. D* 106 (12 Dec. 2022), p. 123032. doi: [10.1103/PhysRevD.106.123032](https://doi.org/10.1103/PhysRevD.106.123032).
992 URL: <https://link.aps.org/doi/10.1103/PhysRevD.106.123032>.
- 993 [28] F. et al. Aharonian. “Observations of the Crab Nebula with H.E.S.S.”. In: *Astron. Astrophys.*
994 457 (2006), pp. 899–915. doi: [10.1051/0004-6361:20065351](https://doi.org/10.1051/0004-6361:20065351). arXiv: [astro-ph/0607333](https://arxiv.org/abs/astro-ph/0607333).
- 996 [29] J. Albert et al. “VHE γ -Ray Observation of the Crab Nebula and its Pulsar with the MAGIC
997 Telescope”. In: *The Astrophysical Journal* 674.2 (Feb. 2008), p. 1037. doi: [10.1086/525270](https://doi.org/10.1086/525270). URL: <https://dx.doi.org/10.1086/525270>.
- 999 [30] N. Park. “Performance of the VERITAS experiment”. In: *Proceedings, 34th International
1000 Cosmic Ray Conference (ICRC2015): The Hague, The Netherlands, July, 30th July - 6th
1001 August*. Vol. 34. 2015, p. 771. arXiv: [1508.07070 \[astro-ph.IM\]](https://arxiv.org/abs/1508.07070).
- 1002 [31] A. Abramowski et al. “H.E.S.S. constraints on Dark Matter annihilations towards the Sculptor
1003 and Carina Dwarf Galaxies”. In: *Astropart. Phys.* 34 (2011), pp. 608–616. doi: [10.1016/j.astropartphys.2010.12.006](https://doi.org/10.1016/j.astropartphys.2010.12.006). arXiv: [1012.5602 \[astro-ph.HE\]](https://arxiv.org/abs/1012.5602).
- 1005 [32] A. Abramowski et al. “Search for dark matter annihilation signatures in H.E.S.S. observations
1006 of Dwarf Spheroidal Galaxies”. In: *Phys. Rev. D* 90 (2014), p. 112012. doi: [10.1103/PhysRevD.90.112012](https://doi.org/10.1103/PhysRevD.90.112012). arXiv: [1410.2589 \[astro-ph.HE\]](https://arxiv.org/abs/1410.2589).
- 1008 [33] H. Abdalla et al. “Searches for gamma-ray lines and ‘pure WIMP’ spectra from Dark
1009 Matter annihilations in dwarf galaxies with H.E.S.S”. in: *JCAP* 11 (2018), p. 037. doi:
1010 [10.1088/1475-7516/2018/11/037](https://doi.org/10.1088/1475-7516/2018/11/037). arXiv: [1810.00995 \[astro-ph.HE\]](https://arxiv.org/abs/1810.00995).

- 1011 [34] J. Aleksić et al. “Optimized dark matter searches in deep observations of Segue 1 with
1012 MAGIC”. in: *JCAP* 1402 (2014), p. 008. doi: [10.1088/1475-7516/2014/02/008](https://doi.org/10.1088/1475-7516/2014/02/008).
1013 arXiv: [1312.1535 \[hep-ph\]](https://arxiv.org/abs/1312.1535).
- 1014 [35] V.A. Acciari et al. “Combined searches for dark matter in dwarf spheroidal galaxies observed
1015 with the MAGIC telescopes, including new data from Coma Berenices and Draco”. In: *Physics of the Dark Universe* (2021), p. 100912. ISSN: 2212-6864. doi: <https://doi.org/10.1016/j.dark.2021.100912>. URL: <https://www.sciencedirect.com/science/article/pii/S2212686421001370>.
- 1019 [36] M. L. Ahnen et al. “Indirect dark matter searches in the dwarf satellite galaxy Ursa Major II
1020 with the MAGIC Telescopes”. In: *JCAP* 1803.03 (2018), p. 009. doi: [10.1088/1475-7516/2018/03/009](https://doi.org/10.1088/1475-7516/2018/03/009). arXiv: [1712.03095 \[astro-ph.HE\]](https://arxiv.org/abs/1712.03095).
- 1022 [37] S. et al. Archambault. “Dark matter constraints from a joint analysis of dwarf Spheroidal
1023 galaxy observations with VERITAS”. in: *prd* 95.8 (Apr. 2017). doi: [10.1103/PhysRevD.95.082001](https://doi.org/10.1103/PhysRevD.95.082001). arXiv: [1703.04937 \[astro-ph.HE\]](https://arxiv.org/abs/1703.04937).
- 1025 [38] Louise Oakes et al. “Combined Dark Matter searches towards dwarf spheroidal galaxies with
1026 Fermi-LAT, HAWC, HESS, MAGIC and VERITAS”. in: *Proceedings of Science*. 2019.
- 1027 [39] Celine Armand et al. on behalf of the Fermi-LAT, HAWC, HESS, MAGIC, VERITAS.
1028 “Combined Dark Matter searches towards dwarf spheroidal galaxies with Fermi-LAT,
1029 HAWC, HESS, MAGIC and VERITAS”. in: *Proceedings of Science*. 2021.
- 1030 [40] Daniel Kerszberg et al. on behalf of the Fermi-LAT, HAWC, HESS, MAGIC, and VER-
1031 TIAS collaborations. “Search for dark matter annihilation with a combined analysis of
1032 dwarf spheroidal galaxies from Fermi-LAT, HAWC, H.E.S.S., MAGIC and VERITAS”. in:
1033 *Proceedings of Science*. 2023.
- 1034 [41] A. U. Abeysekara et al. “Observation of the Crab Nebula with the HAWC Gamma-Ray
1035 Observatory”. In: *The Astrophysical Journal* 843.1 (June 2017), p. 39. doi: [10.3847/1538-4357/aa7555](https://doi.org/10.3847/1538-4357/aa7555). URL: <https://doi.org/10.3847/1538-4357/aa7555>.
- 1037 [42] Giacomo Vianello et al. *The Multi-Mission Maximum Likelihood framework (3ML)*. 2015.
1038 arXiv: [1507.08343 \[astro-ph.HE\]](https://arxiv.org/abs/1507.08343).
- 1039 [43] Marco Cirelli et al. “PPPC 4 DM ID: a poor particle physicist cookbook for dark matter
1040 indirect detection”. In: *Journal of Cosmology and Astroparticle Physics* 2011.03 (Mar.
1041 2011). ISSN: 1475-7516. doi: [10.1088/1475-7516/2011/03/051](https://doi.org/10.1088/1475-7516/2011/03/051). URL: <http://dx.doi.org/10.1088/1475-7516/2011/03/051>.
- 1043 [44] Alex Geringer-Sameth, Savvas M. Koushiappas, and Matthew Walker. “DWARF GALAXY
1044 ANNIHILATION AND DECAY EMISSION PROFILES FOR DARK MATTER EXPERI-
1045 MENTS”. in: *The Astrophysical Journal* 801.2 (Mar. 2015), p. 74. ISSN: 1538-4357. doi:

- 1046 1047 [45] A. Albert et al. “Dark Matter Limits from Dwarf Spheroidal Galaxies with the HAWC
1048 Gamma-Ray Observatory”. In: *The Astrophysical Journal* 853.2 (Feb. 2018), p. 154. ISSN:
1049 1538-4357. doi: [10.3847/1538-4357/aaa6d8](https://doi.org/10.3847/1538-4357/aaa6d8). URL: <http://dx.doi.org/10.3847/1538-4357/aaa6d8>.
- 1050 1051 [46] V. Bonnivard et al. “Spherical Jeans analysis for dark matter indirect detection in dwarf
1052 spheroidal galaxies - Impact of physical parameters and triaxiality”. In: *Mon. Not. Roy.
1053 Astron. Soc.* 446 (2015), pp. 3002–3021. doi: [10.1093/mnras/stu2296](https://doi.org/10.1093/mnras/stu2296). arXiv:
1054 [1407.7822 \[astro-ph.HE\]](https://arxiv.org/abs/1407.7822).
- 1055 1056 [47] Alex Geringer-Sameth and Matthew Koushiappas Savvas M. and Walker. “Dwarf galaxy
1057 annihilation and decay emission profiles for dark matter experiments”. In: *Astrophys.
1058 J.* 801.2 (2015), p. 74. doi: [10.1088/0004-637X/801/2/74](https://doi.org/10.1088/0004-637X/801/2/74). arXiv: [1408.0002
1059 \[astro-ph.CO\]](https://arxiv.org/abs/1408.0002).
- 1060 1061 [48] M. Ackermann et al. “Searching for Dark Matter Annihilation from Milky Way Dwarf
1062 Spheroidal Galaxies with Six Years of Fermi Large Area Telescope Data”. In: *prl* 115.23,
1063 231301 (Dec. 2015), p. 231301. doi: [10.1103/PhysRevLett.115.231301](https://doi.org/10.1103/PhysRevLett.115.231301). arXiv:
[1503.02641 \[astro-ph.HE\]](https://arxiv.org/abs/1503.02641).
- 1064 1065 [49] A. et al. Albert. “Searching for Dark Matter Annihilation in Recently Discovered Milky Way
1066 Satellites with Fermi-LAT”. in: *Astrophys. J.* 834.2 (2017), p. 110. doi: [10.3847/1538-4357/834/2/110](https://doi.org/10.3847/1538-4357/834/2/110). arXiv: [1611.03184 \[astro-ph.HE\]](https://arxiv.org/abs/1611.03184).
- 1067 1068 [50] Mattia Di Mauro and Martin Wolfgang Winkler. “Multimessenger constraints on the dark
1069 matter interpretation of the Fermi-LAT Galactic Center excess”. In: *prd* 103.12, 123005
1070 (June 2021), p. 123005. doi: [10.1103/PhysRevD.103.123005](https://doi.org/10.1103/PhysRevD.103.123005). arXiv: [2101.11027
\[astro-ph.HE\]](https://arxiv.org/abs/2101.11027).
- 1071 1072 [51] V. Bonnivard et al. “Dark matter annihilation and decay in dwarf spheroidal galaxies: The
1073 classical and ultrafaint dSphs”. In: *Mon. Not. Roy. Astron. Soc.* 453.1 (2015), pp. 849–867.
doi: [10.1093/mnras/stv1601](https://doi.org/10.1093/mnras/stv1601). arXiv: [1504.02048 \[astro-ph.HE\]](https://arxiv.org/abs/1504.02048).
- 1074 1075 [52] Gianfranco Bertone, Dan Hooper, and Joseph Silk. “Particle dark matter: evidence, can-
1076 didates and constraints”. In: *Physics Reports* 405.5-6 (Jan. 2005), pp. 279–390. ISSN:
1077 0370-1573. doi: [10.1016/j.physrep.2004.08.031](https://doi.org/10.1016/j.physrep.2004.08.031). URL: <http://dx.doi.org/10.1016/j.physrep.2004.08.031>.
- 1078 1079 [53] HongSheng Zhao. “Analytical models for galactic nuclei”. In: *Mon. Not. Roy. Astron. Soc.*
1080 278 (1996), pp. 488–496. doi: [10.1093/mnras/278.2.488](https://doi.org/10.1093/mnras/278.2.488). arXiv: [astro-ph/9509122
\[astro-ph\]](https://arxiv.org/abs/astro-ph/9509122).

- 1081 [54] H. C. Plummer. “On the Problem of Distribution in Globular Star Clusters: (Plate 8.)”
1082 In: *Monthly Notices of the Royal Astronomical Society* 71.5 (Mar. 1911), pp. 460–470.
1083 ISSN: 0035-8711. doi: [10.1093/mnras/71.5.460](https://doi.org/10.1093/mnras/71.5.460). eprint: <https://academic.oup.com/mnras/article-pdf/71/5/460/2937497/mnras71-0460.pdf>. URL:
1084 <https://doi.org/10.1093/mnras/71.5.460>.
- 1085
1086 [55] Daniel R. Hunter. “Derivation of the anisotropy profile, constraints on the local velocity
1087 dispersion, and implications for direct detection”. In: *JCAP* 02 (2014), p. 023. doi:
1088 [10.1088/1475-7516/2014/02/023](https://doi.org/10.1088/1475-7516/2014/02/023). arXiv: [1311.0256 \[astro-ph.CO\]](https://arxiv.org/abs/1311.0256).
- 1089 [56] Barun Kumar Dhar and Liliya L. R. Williams. “Surface mass density of the Einasto family
1090 of dark matter haloes: are they Sersic-like?” In: *Mon. Not. Roy. Astron. Soc.* (2010). doi:
1091 [10.1111/j.1365-2966.2010.16446.x](https://doi.org/10.1111/j.1365-2966.2010.16446.x).
- 1092 [57] M. Baes and E. Van Hese. “Dynamical models with a general anisotropy profile”. In: *Astron. Astrophys.* 471 (2007), p. 419. doi: [10.1051/0004-6361:20077672](https://doi.org/10.1051/0004-6361:20077672). arXiv:
1093 [0705.4109 \[astro-ph\]](https://arxiv.org/abs/0705.4109).
- 1094
1095 [58] Matthew G. Walker, Edward W. Olszewski, and Mario Mateo. “Bayesian analysis of re-
1096 solved stellar spectra: application to MMT/Hectochelle observations of the Draco dwarf
1097 spheroidal”. In: *mnras* 448.3 (Apr. 2015), pp. 2717–2732. doi: [10.1093/mnras/stv099](https://doi.org/10.1093/mnras/stv099).
1098 arXiv: [1503.02589 \[astro-ph.GA\]](https://arxiv.org/abs/1503.02589).